Propagation of interplanetary (IP) shocks near the Earth

Masatoshi Yamauchi[1,*], Yoshihiro Yokoyama[2,*], Tsubasa Kotani[3], and Jürgen Matzka[4]

[1]Swedish Institute of Space Physics, Kiruna, Sweden
[2]Department of Physics and Technology, UiT The Arctic University of Norway, Tromsø, Norway
[3]Data Analysis Center for Geomagnetism and Space Magnetism, Graduate School of Science, Kyoto University, Kyoto, Japan
[4]GFZ Helmholtz Centre for Geosciences, Potsdam, Germany
[*]This author contributed equally to this work.

Correspondence: M.Yamauchi (M.Yamauchi@irf.se)

Abstract. Solar wind values monitored at the Sun-Earth L1 point have been used to estimate the Earth-arrival time of interplanetary (IP) shocks associated with coronal mass ejections (CMEs) and co-rotating interaction regions (CIRs). In standard estimates, including NASA/OMNI database, the radial propagation speed of the IP shock is assumed to be the same as the measured solar wind (proton) speed after the shock, although these speeds are known to be different in both the shock theory and CME observations. To diagnose the actual differences between these speeds, we statistically compared them using spacecraft data at L1. The propagation speed is obtained from the time-of-propagation between the IP shock passage at the L1 monitoring point and the geomagnetic sudden commencement (SC) at the Earth. As the L1 monitoring point, we use three locations: two are the spacecraft (SOHO and ACE) locations, and the other is the estimated IP shock passage point upstream of the Earth nearest to $Y = Z = 0$ in Geocentric Solar Ecliptic (GSE) coordinate that is calculated from timings and locations of the IP shock passage at both spacecraft (we call the triangle method). In statistics, we limited to the IP shocks with a clear geomagnetic SC signature and with velocity profiles consistent between SOHO and ACE. During 1998-2022, 375 IP shocks satisfied such conditions. For the solar wind speed ($V_{\rm SW}$), the highest value during 15 min after the IP shock passage observed by the selected spacecraft (SOHO or ACE) was used. We found the following tendencies. (1) As expected from the shock theory, arrival time of the IP shock to the Earth (represented by the geomagnetic SC) is earlier than the predicted arrival time of the shocked solar wind by $0-8$ min. (2) The speed difference between the shock propagation and $V_{\rm SW}$ after the shock (highest value during 15 min) is about $+7\%$ compared to SOHO observation and $+10\%$ compared to ACE observation. (3) Tilt angle of the shock estimated by simple 1D shock model using velocity changes across the shock of ACE gives, although this method has large instrumental uncertainty, generally consistent values what is estimated by triangle method within the uncertainty.

1 Introduction

In solar-terrestrial physics including the relevant magnetospheric physics and space weather predictions, upstream monitoring of the solar wind parameters such as the velocity, density, and the interplanetary magnetic field (IMF) is essential. The upstream measurements of these values have been continuously made by monitoring spacecraft at the Sun-Earth Lagrange L1 region for nearly three decades by Wind (Oglivie et al., 1995), SOHO (Ipavich et al., 1998) and ACE (McComas et al., 1998) , and one

decade by DSCOVR. With solar wind velocity and distance between these spacecraft and the Earth, one can roughly estimate the arrival time of the coronal mass ejection (CME) and other large changes in these parameters, such as interplanetary (IP) shocks and large IMF changes.

In these estimates of the arrival time, such as 1-min OMNI data at NASA Omniweb site (https://omniweb.gsfc.nasa.gov/) in which the solar wind data is projected at the Earth's bow shock nose location, the earthward propagation speed of the CME and other IP shocks along the Geocentric Solar Ecliptic (GSE) coordinate $-X_{\rm GSE}$ direction is normally assumed to be the same as the solar wind speed (anti-sunward proton speed) after the shock that is measured at L1 (King and Papitashvili, 2026). However, the propagation speed of the IP shocks is known to be different from the solar wind speed in both the shock theory and CME observations.

For observation near the Sun, the CME front identified by SOHO LASCO imager sometimes propagates at velocity >1000 km/s, being much faster than the solar wind velocity measured at L1 (e.g., Manoharan et al., 2001; Yashiro et al., 2004; Tokumaru et al., 2006; Gonzalez-Esparza and Aguilar-Rodriguez, 2009; Gopalswamy et al., 2009). Although the CME propagation is decelerated while the solar wind is accelerated with distance from the Sun, the IP shocks propagate faster than the solar wind even near the Earth.

In 1D shock models, the conservation of the mass flux across the shock in the shock-rest frame (Rankine-Hugoniot relation) requires that the higher-density side (solar wind after the IP shock passage for forward shock) should have lower relative velocity to the shock. This condition can be achieved only if the shock speed is higher than the solar wind speed (see Fig. A1 in Appendix A for this textbook type relation).

Theoretically, the shock propagation speed should be able to be derived from the measured changes in velocity and density. However, the observation of density, particularly its large increase, is often erroneous right after the IP shocks, causing such a calculated result unreliable (cf. Sect. 2.2 and Appendix A2). This is one of the reasons why the solar wind speed is used for predicting the arrival time of the IP shocks at the Earth. Furthermore, the actual IP shocks are not as ideal as simple models(e.g., local inhomogeneity or wavy structures, which makes even the local shock normal direction different from the large-scale normal direction), and it is wise to avoid using local 1D model in automated prediction of the large-scale propagation.

The time difference comes also from obliquely directed shock front surface ("phase plane") because the location of the monitor spacecraft (SOHO, ACE, and DSCOVR) is largely offset in the GSE Y-Z direction from the Sun-Earth line (Richardson and Paularena, 1998; Collier et al., 1998), at distances up to $\sim 3\times10^5$ km for ACE (https://izw1.caltech.edu/ACE/ASC/DATA/browse-html/y_z_plot.gif) and up to $\sim 7\times10^5$ km for SOHO (https://soho.nascom.nasa.gov/about/orbit.html) away from the Sun-Earth line in the huge L1 region. In such cases, the passage time of the IP shock at the same $X_{\rm GSE}$ location as the monitoring spacecraft can be significantly earlier or later than those at the monitoring spacecraft, causing the estimation error in the predicted arrival time of the IP shock at the Earth. Fortunately, both SOHO and ACE take nearly symmetric orbits with respect to the Sun-Earth line (i.e., in the GSE Y-Z direction). Therefore, the statistical average of the actual arrival time is expected to converge to the expected arrival time, unlike the time difference coming from the difference in speeds.

Since the arrival time of the IP shocks to the Earth is one essential information in understanding the solar wind-magnetosphere interaction including the space weather prediction, it is quite important to examine the degree of difference between the radial

propagation speed of IP shocks (particularly of CMEs) and the speed of the solar wind near the Earth. This type of difference has been reported for the transit time of the IMF changes (e.g., Collier et al., 1998; Milan et al., 2022), but less well studied for the IP shocks (e.g., Paularena et al., 1998, 1999). Particularly, no statistical study on the difference in the speed (between the IP shock propagation and solar wind) near the Earth was made, although the statistical study is mandatory from the above reasons.

The purpose of this paper is to statistically examine the velocity difference between the IP shock propagation and solar wind speed (accordingly, the difference in the arrival time to the Earth) using the solar wind data from the L1 monitoring spacecraft (both SOHO and ACE) and the geomagnetic data. From solar wind data, we obtained the timing of the IP shock passage ($T_{\rm soho}$ for SOHO and $T_{\rm ace}$ for ACE) at the spacecraft location and the solar wind speed ($V_{\rm SW}$) after the IP shock passage, whereas we used geomagnetic data to determine the timing of the geomagnetic sudden commencement (SC) as the proxy of the arrival time of the IP shock to the Earth ($T_{\rm SC}$). Decades of L1 monitoring by SOHO (since 1996) and ACE (since 1997) allows us to take statistics on the difference in speed between the IP shock propagation and the solar wind, using a sufficient number of IP shocks that are identified in both spacecraft with clear geomagnetic SC signatures.

2 Data and Method

Located at the Sun-Earth L1 point, which is about 1.5×10^6 km upstream of the Earth, SOHO and ACE monitor the upstream solar wind. The time resolution of the solar wind data that we used is about 30s for SOHO and 1 min for ACE, and that for the timing of the geomagnetic SC ($T_{\rm SC}$) is also 1 min. Technical descriptions of the solar wind monitoring instruments are found in Ipavich et al. (1998) for SOHO and McComas et al. (1998) for ACE. One important caution that we must raise is the instrument resolution and sensitivity, as summarized in Sect. 2.2 below. Although we conventionally call L1 "point", all L1 monitoring spacecraft take the semi-periodical halo orbit around L1, which covers much larger areas than the size of the Earth (radius of 0.07×10^5 km): the distance from the L1 point in the GSE Y-Z plane can be up to 7×10^5 km for SOHO (https://soho.nascom.nasa.gov/about/orbit.html) and 3×10^5 km for ACE (https://izw1.caltech.edu/ACE/ASC/DATA/browse-html/y_z_plot.gif).

We start from the IP shock list of SOHO (https://space.umd.edu/pm/figs/history.html) and manually examined the velocity profile during 1996-2022 for SOHO and 1998-2022 for ACE. The solar wind data and spacecraft locations are obtained from the NASA Omniweb site (https://cdaweb.gsfc.nasa.gov/). We examined these data to obtain both the timing of the IP shock and the solar wind velocity. We limit the IP shocks to those that are not contaminated by high-speed periods before the IP shock. Among them, we selected those that also caused a clear geomagnetic SC signature, which indicates the arrival of the IP shock to the Earth. All these filtering are done by manually.

The geomagnetic SC is a sudden increase in the horizontal (H) component in the dayside stations that propagates quickly to the nightside (e.g., Araki, 1977; 1994). The propagation time of the SC signature from the magnetopause to the Earth, which is 1-3 min, is about the same as the travelling time of the solar wind from the magnetopause to the Earth's terminator, and their differences are even less. Therefore, we can safely use the onset time of the geomagnetic SC ($T_{\rm SC}$) as a proxy of arrival time of the IP shock to the Earth (e.g., Earth's terminator) in statistics (see Sect. 4.3 for more discussion).

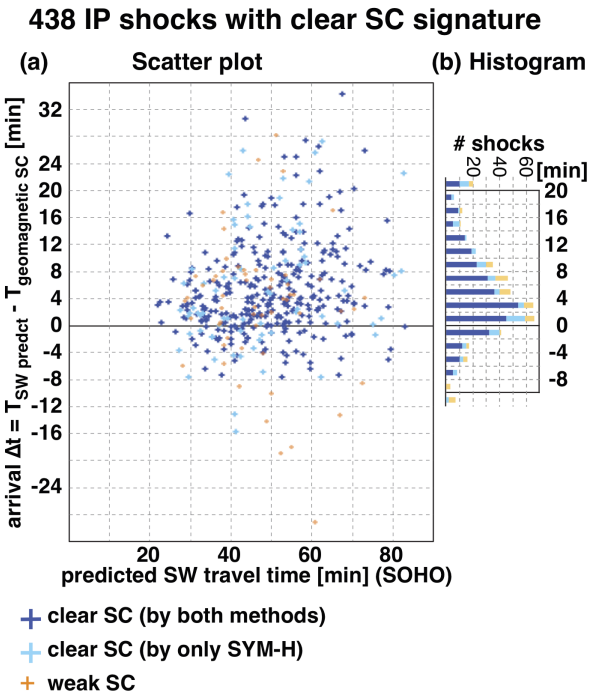

Figure 1. (a) Scatter plot of Δt against the predicted travel time in the $-X_{\rm GSE}$ direction (from SOHO to the Earth) for 438 IP shocks in which the IP shock and geomagnetic sudden commencement (SC) are one-to-one connected. Positive Δt means that the actual arrival of the IP shock to the Earth is earlier than the predicted arrival time using the solar wind speed measured by SOHO. The data are classified into three types in terms of clearness of the SC signature: dark blue, light blue, and orange represent those when the SC is clearly identified in the SYM-H index while it is also found in the SC list at Ebre Observatory (https://www.obsebre.es/en/variations/rapid), only in the SYM-H index, and only with weak or unclear SC signatures (e.g., amplitude less than 10 nT in SYM-H index or signature during some on-going activity), respectively. (b) Histogram of the time difference Δt, which is the same as the integration of panel (a) over all the travel time. The same colors are used for the sub-classified types.

In this method of estimating the arrival time of the IP shock, the geomagnetic variation is sometimes contaminated by on-going geomagnetic activities (this can also be examined by the geomagnetic AE index). Therefore, we also limit to the cases when the geomagnetic SC is clearly identified in SYM-H index (e.g., Nanjo et al., 2025), which is provided by WDC for geomagnetism, Kyoto (https://wdc.kugi.kyoto-u.ac.jp/aeasy/index.html). This gives us 438 examples out of more than 650 IP shocks in the list. To confirm our list of the geomagnetic SC, we also used the SC list provided by the Ebre Observatory (https://www.obsebre.es/en/variations/rapid), in which the magnetometer data from five longitudinally distributed low-latitude stations are used to identify the geomagnetic SC.

Fig. 1 shows the distribution of the time difference (Δt) between the expected arrival time of the shock-related solar wind and actual arrival time represented by the geomagnetic SC ($T_{\rm SC}$) detected in SYM-H. Positive Δt means earlier $T_{\rm SC}$ than the expected arrival of the solar wind. When estimating the travel time of the solar wind, we used the maximum value of the solar

wind speed within 15 min after the IP shock passage because widening of the energy range and high count rate in the shocked solar wind can make the velocity value unstable (or underestimated due to saturation) in the actual detection by the instrument (cf. Sect. 2.2). The duration of 15 min is sufficient for not missing the real peak value of fluctuating speed while it is short enough excluding independent velocity increase afterward, according to our manual examination of all the velocity plots of the IP shock passages.

In Fig. 1, left panel (a) shows a scatter plot of Δt against the predicted travel time of the shocked solar wind (from SOHO to the Earth) in the $X_{\rm GSE}$ direction; and right panel (b) shows the number of IP shocks at different Δt bin. Different colors in Fig. 1 (dark blue, light blue, and orange) represent different clearness of the SC signature (see the figure caption). As is expected from two reasons mentioned in the Introduction (1D shock theory and oblique propagation), Fig. 1 shows large spread in Δt, with the majority of the cases having $\Delta t > 0$.

Fig. 1 includes IP shocks that are quite non-uniform in the GSE Y-Z direction. In fact, the velocity profile and particularly the density profile are often different between SOHO and ACE. Considering that the large location difference between SOHO and ACE can be as large as 3×10^5 km in the $X_{\rm GSE}$ direction and 7×10^5 km in the GSE Y-Z direction, it is not surprising that the non-uniform structure of the IP shock makes such SOHO-ACE differences. While the SOHO–ACE density differences might be attributed to the different measurement methods of the solar wind protons between SOHO and ACE (ACE generally has a saturation threshold at lower flux than SOHO), the inter-spacecraft difference in the velocity profile mainly comes from the non-uniform structure of the IP shock.

To remove such non-uniform cases, we further limit to cases when the velocity profiles are consistent between SOHO and ACE with a clear IP shock signature (e.g., the velocity is relatively stable before the IP shock as mentioned above), according to our manual examination of the velocity profiles. This gives us 375 "consistent" examples out of these 438 IP shocks during 1998-2022, for which we can assume that both spacecraft detected the same IP shock.

2.1 Estimating the anti-sunward shock propagation speed

In this study, we examine two parameters using these 375 IP shocks. The first parameter is the time difference Δt, as mentioned above, using the highest value of the solar wind speed during 15 min after the IP shock passage. The second parameter is the estimated anti-sunward propagation speed of the IP shock in the $-X_{\rm GSE}$ direction. We use two methods. (a) Single-spacecraft timing method ($V_{\rm timing}$): the speed is derived from the timing of the IP shock detection by one spacecraft ($T_{\rm soho}$ for SOHO or $T_{\rm ace}$ for ACE) and its $X_{\rm GSE}$ location by assuming that the shock normal points in the $-X_{\rm GSE}$ direction. (b) Triangle method ($V_{\rm triangle}$): the speed is derived from timings of the shock passage by assuming a 1D shock front that is tilted by angle θ_η in the η direction. Since we use only two spacecraft in this study, the triangle method can estimate the tilt angle only in the η direction (two spacecraft alignment direction as shown in Fig. 2a) and not angle θ_ζ in the other ζ direction in Fig. 2a.

A general triangle method for closely-located multi-spacecraft observation is given in Paschmann and Daly (1999) (Chapter 10, 11), but that does not consider the application to the L1 monitoring spacecraft where (a) inhomogeneity of the shock front makes local propagation speed quite different from large-scale propagation speed, and (b) limited angular resolution of the ion instruments make large error in the velocity measurement in the GSE Y–Z direction as described in Sect. 2.2. Instead, we take

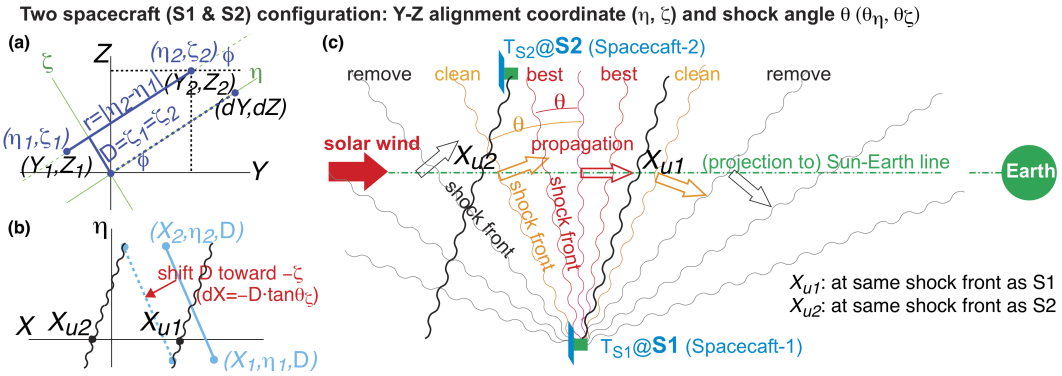

Figure 2. (a) Definition of the η–ζ coordinate based on the alignment of two spacecraft looking from the Sun toward the Earth (looking from $+X_{\rm GSE}$). It is rotated by an angle ϕ of the alignment direction from the $Y_{\rm GSE}$ direction. (b) The spacecraft alignment direction at $\zeta = D$ plane (solid blue line) and its projection along the shock surface (tilted by angle θ_ζ) to the $\zeta = 0$ plane (dashed blue line) are shown in the η–ζ coordinate. The shock surface in the $\zeta = 0$ plane is shown by the black wavy lines (which is tilted by angle θ_η). The signs of these angles are defined as the surface normal direction deflected from $-X_{\rm GSE}$ direction toward positive η or positive ζ. (c) General configuration of the IP shocks (wavy lines), propagating (empty arrows) through two spacecraft (S1 and S2) that represent SOHO and ACE. Different colors represent different datasets (best, clean, and consistent) in terms of shock angle (θ_η) that is defined in Fig. 3b.

the following approach that makes the error estimation easy. The geometry and coordinate of this triangle method is illustrated in Fig. 2. Textbook type information on the coordinate transformation from $Y_{\rm GSE}$–$Z_{\rm GSE}$ system to η-ζ system (rotating by angle ϕ in the $Y_{\rm GSE}$–$Z_{\rm GSE}$ plane) is given in Appendix B.

In Fig. 2b configuration, the propagation speed of the IP shock ($V_{\rm shock}$) from the upstream point ($Y_{\rm GSE}$=$Y_{\rm GSE}$=0, or η=ζ=0) to the Earth becomes the same between using the projected SOHO location (and shifted by distance $D = (Z_{\rm soho} \cdot Y_{\rm ace} - Y_{\rm soho} \cdot Z_{\rm ace})/r$ with angle θ_ζ in Fig. 2a) and using the projected ACE location to the upstream point (and shifted by distance D with angle θ_ζ):

$$V_{\rm shock} = [X_{\rm soho} - \eta_{\rm soho} \cdot \tan\theta_\eta - D \cdot \tan\theta_\zeta]/dt_{\rm soho} \\ = [X_{\rm ace} - \eta_{\rm ace} \cdot \tan\theta_\eta - D \cdot \tan\theta_\zeta]/dt_{\rm ace} \quad (1)$$

where the signs of θ_η and θ_ζ are defined positive if the shock surface tilts from $X_{\rm GSE} = constant$ plane toward positive η or positive ζ directions (see Fig. 2 caption), or

$$\tan\theta_\eta = \frac{(X_{\rm soho}/dt_{\rm soho}) - (X_{\rm ace}/dt_{\rm ace})}{(\eta_{\rm soho}/dt_{\rm soho}) - (\eta_{\rm ace}/dt_{\rm ace})} - D \cdot \tan\theta_\zeta \cdot \frac{(1/dt_{\rm soho}) - (1/dt_{\rm ace})}{(\eta_{\rm soho}/dt_{\rm soho}) - (\eta_{\rm ace}/dt_{\rm ace})} \quad (2)$$

For the ζ direction, we have to rely on the other method, such as using a 1D shock model ($\theta_{\zeta 1D}$: Appendix A1), which has a large error range due to (a) inhomogeneity of the shock front that makes the local propagation speed quite different from the large-scale propagation speed, and (b) limited angular resolution of the ion instruments as described in the next subsection (Sect. 2.2). Therefore, in the statistical study, we select examples in which θ_ζ is small compared to the measurement uncertainty

that is described in Sect. 2.2. Fortunately, the second term in Eq. (2) ($D \cdot \tan\theta_\zeta$ term) is less than 0.3 for 99% of 375 shocks (less than 0.1 for 93%). In such cases, angle θ_ζ disappears from Eqs. (1) and (2) as:

$$\tan\theta_\eta \sim \frac{(X_{\rm soho}/dt_{\rm soho}) - (X_{\rm ace}/dt_{\rm ace})}{(\eta_{\rm soho}/dt_{\rm soho}) - (\eta_{\rm ace}/dt_{\rm ace})} \qquad ({\rm for\ D} \ll {\rm r\ or\ small}\ \theta_\zeta) \tag{3}$$

$$V_{\rm triangle} \sim [X_{\rm soho} - \eta_{\rm soho} \cdot \tan\theta_\eta]/dt_{\rm soho} \sim [X_{\rm ace} - \eta_{\rm ace} \cdot \tan\theta_\eta]/dt_{\rm ace} \qquad ({\rm for\ small}\ \theta_\zeta) \tag{4}$$

Using Eqs. (3) and (4), we can obtain $V_{\rm triangle}$ and θ_η only from the timings and locations of the IP shock passage at two spacecraft. In the statistical analyses in this paper, we use these simplified formulae for $V_{\rm triangle}$ and θ_η such that errors in the measured values (see below in Sect. 2.2) do not affect the result.

2.2 Accuracy of measurements

As is always the case with ion instruments, limited dynamic range of the sensor (for SOHO and ACE, it is microchannelplate (MCP)) causes saturation of the signal near and beyond the upper detection limit of the flux (ions entering the instrument too often beyond the sensor's capacity). In very high flux conditions such as during the passage of CME-driven IP shocks, saturation of the sensor causes underestimation of the flux and a shift of the central position in both energy and inflow angle. Among those, the energy (i.e., speed) is relatively well controlled (although the widening of the detecting energy causes some error in the energy) even during high-flux condition. Therefore, an underestimation of flux due to the saturation causes underestimation of the density (which is defined as the flux divided by speed). As shown in Appendix A2 (Fig. A1e), such underestimation causes a significant error in the theoretical propagation velocity when the change in the density is small. Therefore, we do not use density data in this study.

Deflection angle (angle that the solar wind is coming into the instrument, measuring from the Sun direction) is another problem: the three-axis stabilized SOHO can measure the deflection of the solar wind only in the $Z_{\rm GSE}$ direction but not in the $Y_{\rm GSE}$ direction at all (Ipavich et al., 1998). The solar wind instrument on board the spinning ACE spacecraft (spin period 12 sec) has several entrance directions to cover the third direction (mainly in the $Z_{\rm GSE}$ direction), but this 3D design sacrificed the angular resolution to 2.5°–5° in the sector direction (the best resolution requires longer integration time) and 3–4.5° in the spinning direction, both after 1-min integration during stable solar wind conditions (McComas et al., 1998). The resolution during IP shock passage must be worse than these values.

Since $\tan(2.5^\circ) = 4.4\%$ and $\tan(4^\circ) = 7.0\%$, a solar wind velocity of only 450 km/s (low values for the IP shock conditions) already gives 20-30 km/s uncertainty in the deflection (Y–Z) direction. Although NASA/OMNI dataset provides the Y–Z components of the solar wind velocity to the last digit, the uncertainty lies already in the tens of km/s, making the final estimate for the error in the 1D-model shock angle ($\theta_{\eta 1D}$, see Appendix A) quite large. In contrast, the triangle method uses only the timing and location, with the time resolution (1 min) being the controlling factor determining the uncertainty in the estimate of θ_η.

Fig. 3 shows scatter plots that compare the triangle method (horizontal axis) and the 1D-model method (vertical axis). Fig. 3a compares the estimated shock angle in the η direction by the triangle method (θ_η) and the observed change in the solar wind deflection angle across the shock. If we include the instrumental uncertainty in the deflection angle of about 4°(hatched area),

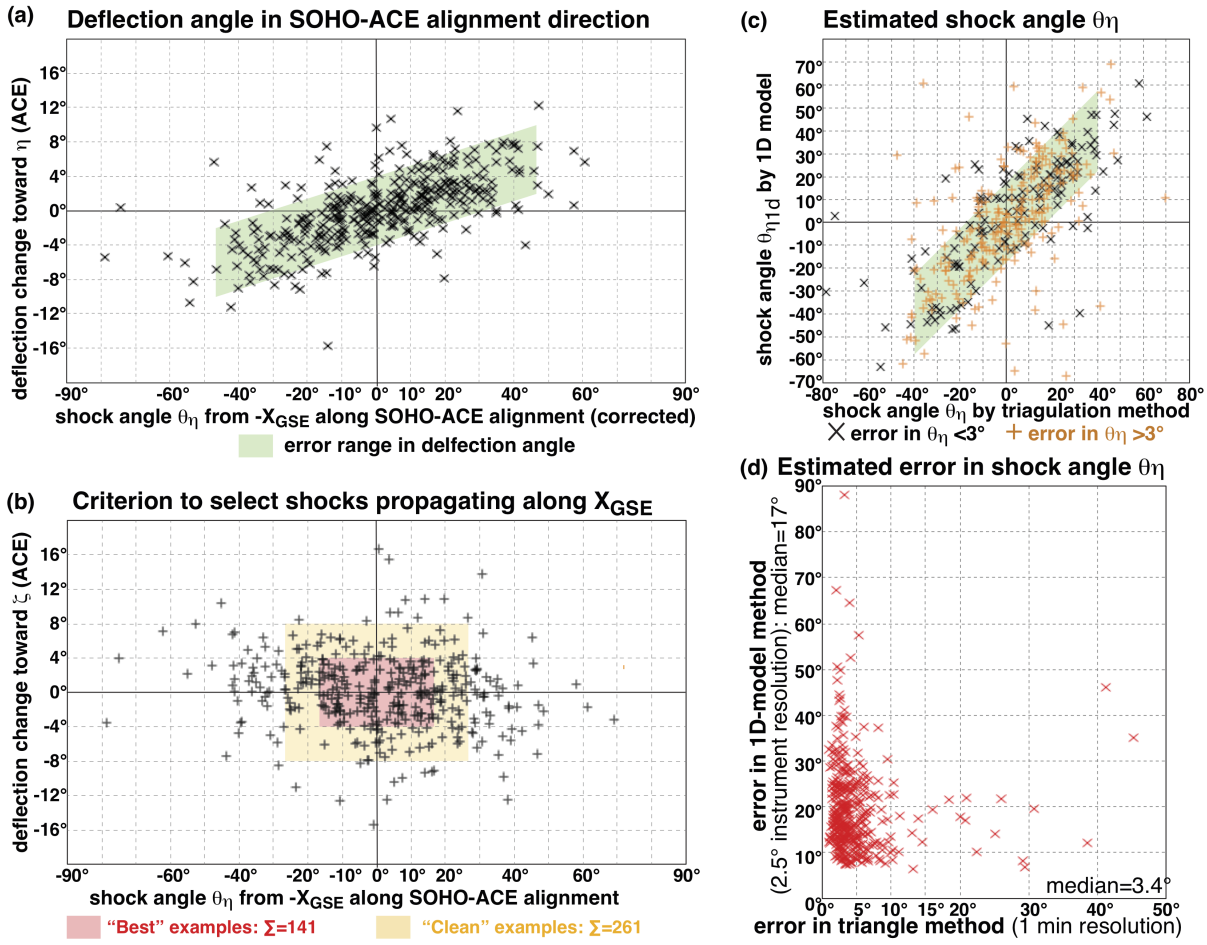

Figure 3. (a) Scatter plot comparing the change in the solar wind deflection angle across the shock in the η direction and the shock angle in the in the η by the triangle method (θ_η, based on Eq. (2)). (b) The same as (a) but for the deflection angle in the ζ direction, while the horizontal axis is the same (θ_η) except using Eq. (3). (c) Scatter plot comparing the shock angles in the η direction $\theta_{\eta 1D}$ and θ_η (based on Eq. (2)). (d) Scatter plot comparing the estimated errors in the shock angle in the η direction. Here we used Eq. (3) to derive the error in θ_η. The deflection angle is the angle that the solar is coming into the instrument measuring from the Sun direction. All three velocity components of the solar wind are calculated using the solar wind speed (eventually the energy) and these angles in the $X_{\rm GSE}$–$Y_{\rm GSE}$ and $X_{\rm GSE}$–$Z_{\rm GSE}$ directions. The hatched area in (a) and (d) shows the "consistent" range between the triangle method (Sect. 2.1) and the 1D-model method (Appendix A1) after considering a 4° degree uncertainty in the deflection angle of the solar wind measurement (and 17° uncertainty in $\theta_{\eta 1D}$). The hatched areas (larger and smaller areas) in (b) shows selection criterions for "clean" and "best" shocks as summarized in Table 1, respectively, in selecting shocks propagating nearly along the $-X_{\rm GSE}$ direction, i.e., small shock angle θ in both η and ζ directions.

185 a majority of the observations is consistent to each other. Therefore, the value of 4° is a good estimate of the actual uncertainty

Table 1. Different subsets of IP shocks

Number of IP shocks	Cleaning level
438 "basic samples"	Clear IP shock & geomagnetic SC are identified by SOHO &SYM-H
375 "consistent" samples out of 438	IP shock profile is consistent between SOHO and ACE
261 "clean" samples out of 375	$\theta_\eta < 26^\circ$ ($\lvert\tan\theta\rvert < 0.5$, $\cos\theta > 0.89$) & change in ζ deflection < 8°
141 "best" samples out of 261	$\theta_\eta < 17^\circ$ ($\lvert\tan\theta\rvert < 0.3$, $\cos\theta > 0.96$) & change in ζ deflection < 4°

in the deflection angle of the solar wind measurement in the η direction. Fig. 3a also indicates that there are many shocks in which uncertainty in the deflection angle may be larger (wider area than the hatched area), as mentioned above.

After converting the change of the deflection angle across the shock to the shock angle by the 1D-model method, both estimates of the shock angle in the η direction (1D-model method $\theta_{\eta 1D}$ and triangle method θ_η) are compared in Fig. 3c. We also estimated the error in these θ_η and $\theta_{\eta 1D}$ by assuming 1-min error in Eq. (2) and 2.5° error (minimum possible error from the instrument design) of deflection angle in Eq. (A2). Fig. 3d shows the result. The estimated uncertainty in the η direction is about five times larger for the 1D-model method than for the triangle method (medium values are 17° for the 1D-model method and 3.4° for the triangle method), contrary to the claim by Toth et al. (2026) who overlooked the large uncertainty in the velocity measurement. This endorses the error estimate of $\theta_{\eta 1D}$ in Fig. 3c (hatched area, about $\pm 20^\circ$ error in $\theta_{\eta 1D}$). Since the uncertainty in the deflection angle comes from the instrumental design, we expect about the same uncertainty even in the ζ deflection angle ($\pm 4^\circ$), and hence in $\theta_{\zeta 1D}$ ($\pm 20^\circ$).

If we have a third spacecraft, we can estimate the shock angle in both directions by the triangle method, but with two spacecraft, we have to relay on the 1D-model method in the ζ direction, which has such a large uncertainty. Fortunately, our purpose is just the large-scale propagation speed of the IP shocks and its uncertainty. Then, it is wise to use the angle information only to extract the "best" examples for which we can assume anti-sunward propagation nearly along the $-X_{\rm GSE}$ direction. Note that the discrepancy between these two methods may also come from the difference between the large-scale shock angle and the small-scale shock angle, e.g., by curvature of the shock surface in both large scale (round) and small scale (wavy).

The hatched area in Fig. 3b shows this criterion for the clean dataset (261 shocks) and the best dataset (141 shocks), which are summarized in Table 1. A list of timings of the IP shock detection and geomagnetic SC for 438 IP shocks, including the classification of the difference sub-datasets, is listed in Appendix C (Tables A1-4). The criterion in the ζ direction is slightly less restrictive than in the η direction because of large error range in the 1D-shock model, because a deflection angle of 4° is about 20° error in the shock angle according to Figs. 3a and 3c.

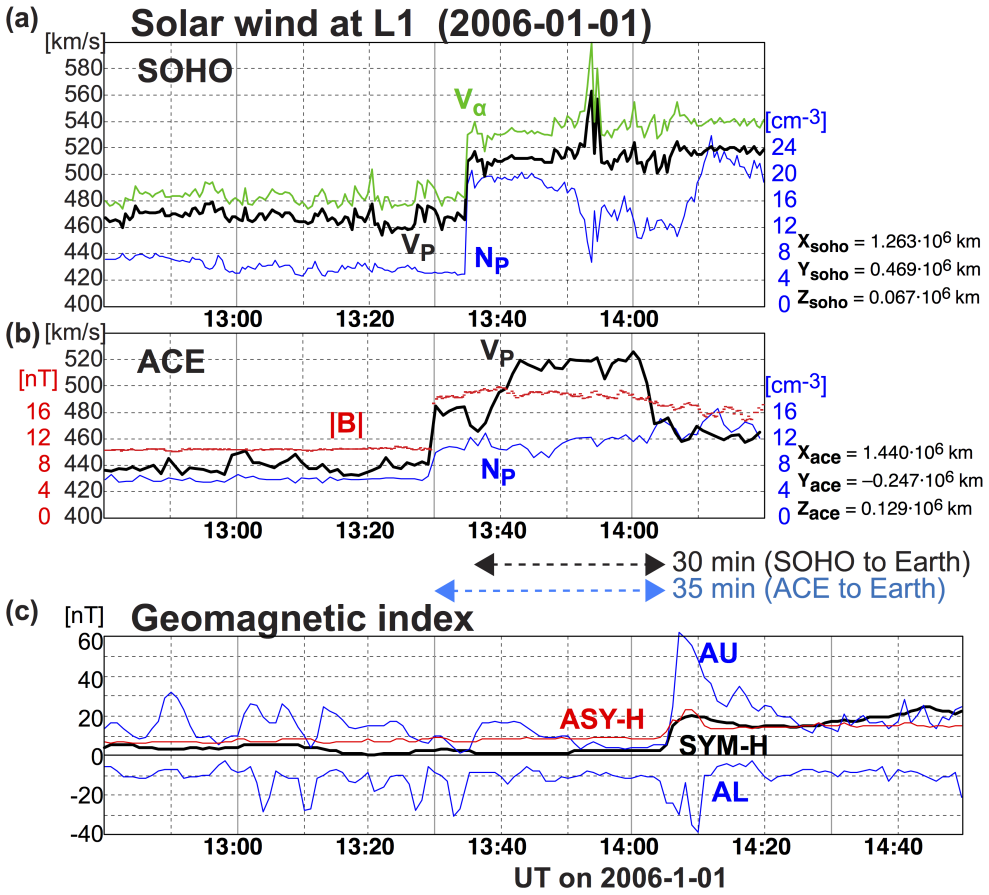

Figure 4. Solar wind data observed by (a) SOHO and (b) ACE for the IP shock event on 2006-01-01. The proton speed, proton density, and the IMF intensity are plotted by thick black lines, thin blue lines, and a thin red line, respectively. As a reference, speed of the alpha particle is also plotted by a green line in the top panel. The IP shock is identified as sudden simultaneous intensification of the density and velocity for both SOHO (13:35 UT) and ACE (13:30 UT). The IMF total field measured by ACE also shows sudden intensification at the same timing (13:30 UT). (c) Geomagnetic indices SYM-H (thick black lines), ASY-H (thin red line), AU and AL (both thin blue lines) for the same IP shock. Sudden increase of SYM-H (and ASY-H and AU) is observed at 14:05 UT.

2.3 Example

Fig. 4 shows an example of clean but not the best IP shock. Figs. 4a and 4b show that a sudden sharp increase in the proton speed (thick black line) and density (thin blue line) occurred simultaneously for both SOHO at 13:35 UT (Fig. 4a) and ACE at 13:30 UT (Fig. 4b) on 2006-01-01. Also, the total IMF strength (dashed red line) observed by ACE suddenly increased simultaneously at 13:30 UT. Since the IP shock timing was identified as a sudden increase in dynamic pressure, the above timing corresponds to the IP shock timing passing through SOHO and ACE, respectively. Fig. 4c shows that SYM-H suddenly increased at 14:05 UT as an isolated geomagnetic SC during a quiet period without any contamination from any magnetospheric

activities (as seen from AU and AL indices). From the above timings, travel time of the IP shock is estimated as $dt_{\rm soho} = 30 \pm 1$ min for SOHO-Earth propagation and $dt_{\rm ace} = 35 \pm 1$ min for ACE-Earth propagation.

Let us estimate the propagation speed of the IP shock in the $-X_{\rm GSE}$ direction. According to the simplified formulae Eqs. (3) and (4) and the location of the spacecraft given in Fig. 4, we have an estimate of $\theta_\eta = 2^\circ \pm 3^\circ$ and $V_{\rm triangle} \sim 690 \pm 10$km/s. This value is even consistent with the propagation speed using only one spacecraft assuming an ideal 1D shock propagating in $-X_{\rm GSE}$ direction. The propagation time of 30 ± 1 min over $X_{\rm soho} = 1.263 \times 10^6$ km means about $\sim 700 \pm 30$ km/s, and 35 ± 1 min over $X_{\rm ace} = 1.440 \times 10^6$ km means about $\sim 690 \pm 20$ km/s). Also, the shock angle estimated by the 1D model ($\theta_{\eta 1D} = 10^\circ \pm 25^\circ$) is consistent with the θ_η value by the triangle method above.

On the other hand, the tilt angle in the ζ direction (only 1D-model method can estimate) gives a large value of $\theta_{\zeta 1D} = 47^\circ \pm 25^\circ$ (the ζ deflection angle of the solar wind is $5.8^\circ \pm 4^\circ$). While the corrected $\theta_\eta = 1^\circ \pm 4^\circ$ according to Eq. (2) is unchanged from the above simplified estimate, corrected $V_{\rm triangle}$ according to Eq. (1) significantly decreased to ~630 km/s with a large error range of $\pm$50km/s (the error range is $\pm$30km/s even if the uncertainty of the deflection angle is 2.5°). Thus, it is wise not to use the derived tilt angle to estimate $V_{\rm triangle}$ but to select the best IP shocks (only small tilt angles), as summarized in Fig. 3b and Table 1.

In this example, the estimated $V_{\rm triangle} \sim 630 \pm 50$km/s is much higher than the maximum solar wind speed of 520 km/s (the same value for both SOHO and ACE) observed within 15 min after the IP shock passage. For reference, we compare with the theoretical propagation speed in a simple 1D shock model (cf. Appendix A), although such an estimate requires density values (can be quite erroneous as discussed in Sect. 2.2). In fact, the density jumps across the shock in Fig. 4 are quite different between SOHO and ACE (nearly 4 times for SOHO and only double for ACE). The speed change is also different (from 470 km/s to 520 km/s for SOHO and 440 km/s to 520 km/s for ACE). Such a difference even suggests that the shock might be inhomogeneous in the η direction, as mentioned in Sect. 2.2.

With these limitations in mind, the estimated phase velocity of the shock in the $-X_{\rm GSE}$ direction according to Eq. (A1) in Appendix A (540 km/s for SOHO and 600 km/s for ACE) is not very reliable While estimation by the ACE data is within the uncertainty range of $V_{\rm triangle}$ by the triangle method (required tile angle is $> 70^\circ$), estimation by the SOHO data is generally more reliable than the ACE estimate as discussed in Sect. 2.2 and Appendix A2.

In summary, the anti-sunward phase speed of the IP shock propagation on the 2006-01-01 event (estimated as ~ 630 km/s) is much faster than the solar wind (~ 520 km/s) as expected from the shock theory. However, we cannot use this example to "test" the theoretical model to derive the propagation speed (of ~ 540 km/s based on SOHO density and velocity observations). The measurement uncertainties in the deflection angle and density are too high to judge if the discrepancy between these estimates comes from inhomogeneity, instrumental limitations, or other unknown reasons. This example encourages statistical examination of the shock propagation speed using the most reliable measurements (timing, distance, and solar wind energy or speed) rather than theoretical estimates using less reliable measurements and extra assumptions.

2.4 Statistical method

The purpose of the paper is to obtain the statistical difference between the shock propagation speed and the solar wind speed. To minimize the uncertainty introduced by the instrumental limitation, we use only the timing of the shock passage and the spacecraft location ($X_{\rm GSE}$, $Y_{\rm GSE}$, $Z_{\rm GSE}$) in calculating the speed. For the same reason, we select ideal IP shocks from the 375 "consistent" examples according to Table 1 and Fig. 3b: those with the shock normal most likely pointing more or less in the $-X_{\rm GSE}$ direction, as illustrated with red and orange empty arrows in Fig. 2c.

We first show the results when the finite $Y_{\rm GSE}$ and $Z_{\rm GSE}$ is ignored (Figs. 5 and 6) because this is what is used for the real-time prediction of the arrival time in the space weather operation. Even with such assumption, we expect that the error introduced by this assumption is expected to be equally distributed to plus side and minus side, and may give some idea how fast the shock propagates compared to the solar wind.

3 Results

Fig. 5 shows the statistics of the time difference Δt for SOHO (left panels) and ACE (middle panels). The format of each panel is the same as Fig. 1b. Figs. 5a and 5d show the distributions of all 375 consistent IP shocks, Figs. 5b and 5e show the distributions of clean subset (261 samples), and Figs. 5c and 5f show the distribution of the best subset (141 samples), as is described in the previous section.

For both SOHO and ACE, Δt values of 375 consistent IP shocks (Figs. 5a and 5d) are distributed wide spread (central 80% range and standard deviations (STD) are -2 to $+15$ min (STD=7.2 min) for SOHO, and $+2$ to $+13$ min (STD=5.6 min) for ACE). The distribution is more compact in the best dataset (Figs. 5c and 5f) with central 80% range -1 min to $+8$ min with STD=4.9 min for SOHO, and $+1$ min to $+9$ min with STD=3.4 min for ACE. The numbers of extreme Δt examples (< -6 min or > 20 min) also decreases from 26 to 3 for SOHO and 11 to 1 for ACE for the best 141 examples compared to the consistent 375 examples. In fact, the removed examples (Fig. 5g) show much flatter distribution than clean and best example, consistent with wide error for oblique shocks as explained in the introduction.

In all panels, the center of Δt is shifted toward the positive side; i.e., the IP shock generally arrives earlier than the predicted arrival time calculated from the measured solar wind speed at L1, as is expected from the shock theory. The earlier arrival of the IP shock to the Earth than the solar wind itself is valid in almost all cases, and negative Δt is most likely a part of spread of the distribution, which is expected as the statistical property of the oblique shock plane, as explained in the introduction.

Fig. 6 shows the velocity ratio $V_{\rm timing}/V_{\rm SW}$ for SOHO (left panels) and ACE (right panels) in the same format as Fig. 5, where $V_{\rm SW}$ is the solar wind proton velocity and $V_{\rm timing}$ is the IP shock's propagation velocity using only one spacecraft (the same assumption as Fig. 5). Since we consider the ratio, we linearized the binning by taking logarithmic scale; i.e., we plotted the distribution against log10($V_{\rm timing}/V_{\rm SW}$). The resultant distributions are similar to those of Δt in Fig. 5.

For the 141 best examples, $V_{\rm timing}$ is -2 to $+18$% (central 80%) faster (negative sign means slower) than the solar wind speed for SOHO ($+3$ to $+19$% for ACE), with the simple average and standard deviation of $log10(V_{\rm timing}/V_{\rm SW})$ as 0.029 and 0.044 ($+7 \pm 11$% difference) for SOHO as shown in Fig. 6c ($+10 \pm 7$% difference for ACE, as shown in Fig. 6f).

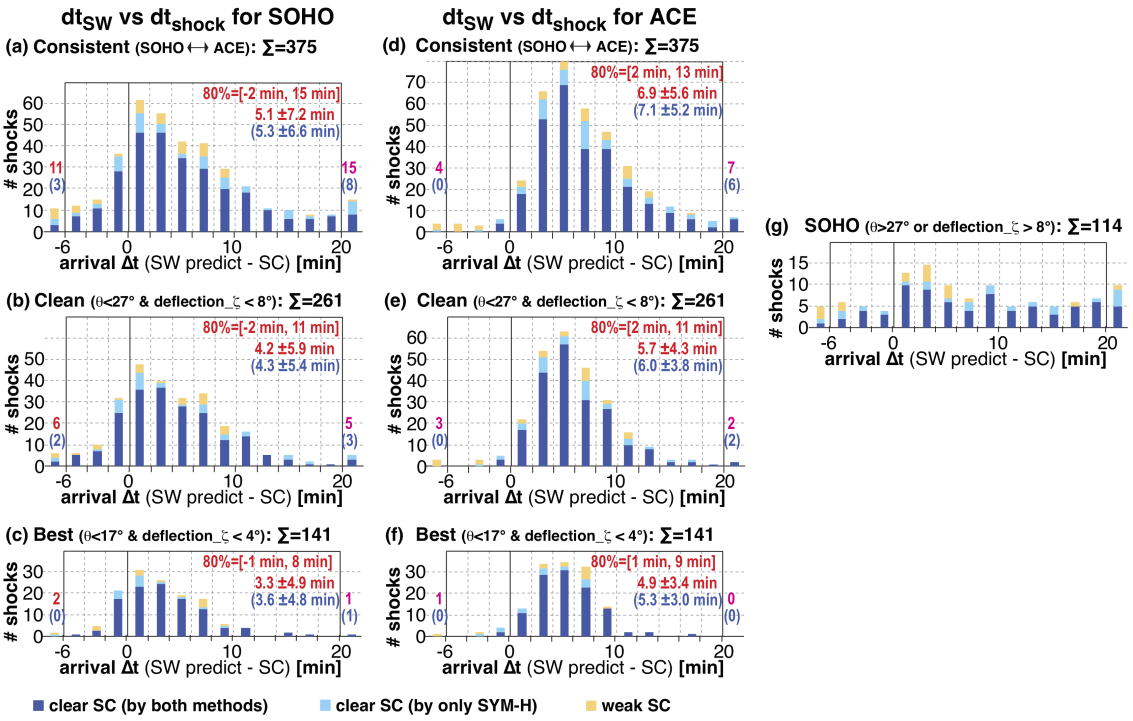

Figure 5. Histogram of the time difference Δt between the arrival times of the IP shock at the Earth using the geomagnetic SC signature in SYM-H ($T_{\rm SC}$), and the expected travel time of the solar wind using the fastest solar wind speed within 15 min from an IP shock for (a)-(c) SOHO and (d)-(f) ACE. Top panels (a) and (c) show the distributions of 375 "consistent" IP shocks, middle panels (b) and (e) show the distributions of 261 "clean" IP shocks, and bottom panels (c) and (f) show the distributions of 141 "best" IP shocks, as defined in Fig. 2 and Table 1. (g) The same histogram for removed samples from (a) to (b) for SOHO, i.e., difference between (a) and (b). In each panel, values at the upper right part show the 80% range of the distribution, followed by the average value and the standard deviation. The values inside the parenthesis represent only those with the geomagnetic SC signature detected by two methods. The values at lower left and right edges show the summation of extreme values for both negative (< -6 min) and positive (> +20 min) sides, respectively. Positive Δt means that the actual arrival of the IP shock to the Earth is earlier than the predicted arrival time using the solar wind speed measured by SOHO or ACE. The data are classified into three types in terms of clearness of the SC signature in the same manner as Fig. 1a.

These averages are unchanged if we use $V_{\rm triangle}$ (which is common for SOHO and ACE) instead of $V_{\rm timing}$ for both SOHO and ACE, as shown in Fig. 7, where the results for $V_{\rm triangle}$ (triangle method using two spacecraft) are shown instead of $V_{\rm timing}$. Even the standard deviation is nearly unchanged by using $V_{\rm triangle}$ (reduced only by 2% for SOHO and unchanged for ACE). However, the distribution with respect to the average value for SOHO case becomes more symmetric (Gaussian-like) by using $V_{\rm triangle}$ than using $V_{\rm timing}$, with a reduced 80% range. Contrary to the SOHO cases (Figs. 7a–7c), ACE data show some asymmetry with respect to its peak, indicating less reliable velocity measurements than SOHO, as discussed in Sect. 2.2.

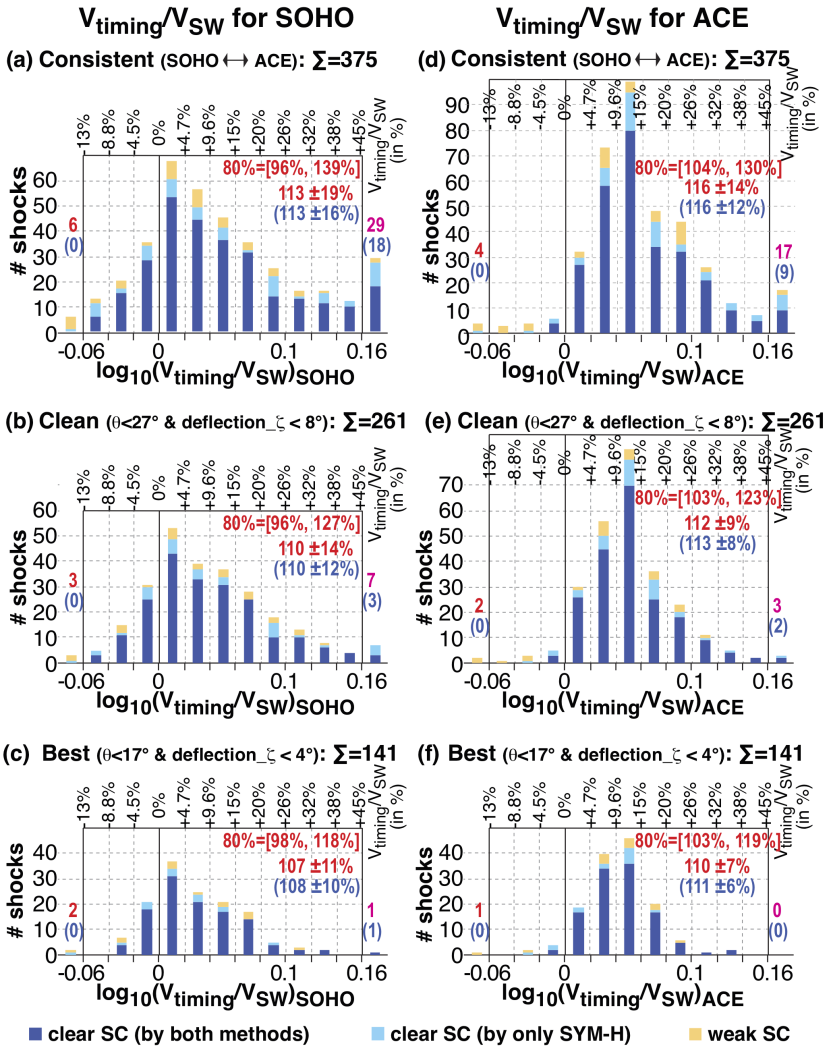

Figure 6. The same as Fig. 5, but for the velocity ratio between the solar wind proton velocity ($V_{\rm SW}$) and the IP shock's propagation velocity ($V_{\rm timing}$). The latter is calculated using the time difference and $X_{\rm GSE}$ distance between the IP shock passage at (a)-(c) SOHO or at (d)-(f) ACE, and the Earth (the geomagnetic SC signature is used for timing at the Earth). To linearize the binning of velocity ratio, we plotted in logarithmic scale. For example, -0.06 and 0.06 correspond to 87% (i.e., 13% slower propagation speed than the solar wind speed) and 115% (i.e., 15% faster), respectively. These differences are written at the top of each panel.

4 Possible error sources

In all estimates using timings at L1 and the Earth to derive the propagation speed (Figs. 6 and 7), the shock propagation is faster than the solar wind flow, as is predicted from the shock theory for the forward shock (cf. Appendix A). The differences in the speed are about 7% (0% to +14% for central 80%) for SOHO and about 10% (+3 % to +17%) for ACE. For such small

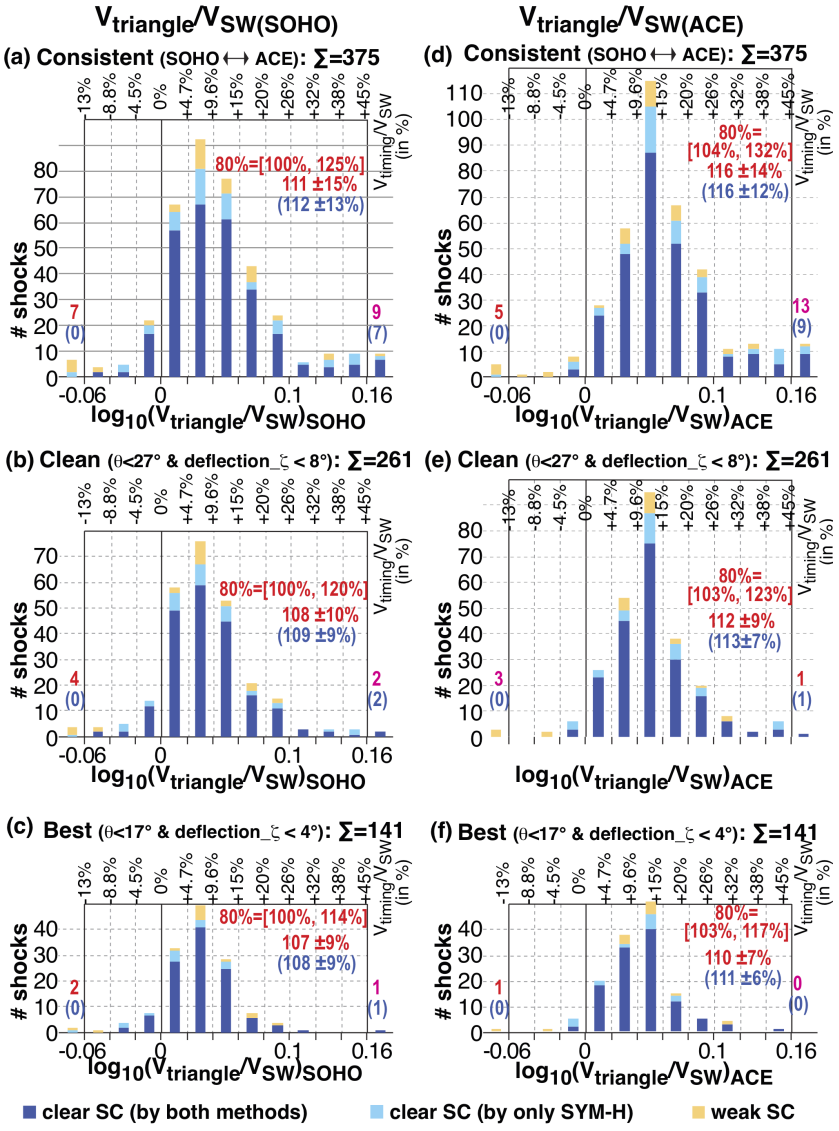

Figure 7. The same as Fig. 6, but instead $V_{\rm timing}$, using $V_{\rm triangle}$ that is estimated according to Eqs. (1) and (2).

differences, we must consider possible sources of the uncertainty in the measurements (solar wind speed and timings) before using this value (about 7% difference compared to the fastest solar wind speed within 15 min after the shock) as the value how fast the shock propagates.

4.1 Velocity value

One question is the accuracy of the velocity values. Although the SOHO proton monitor velocity is well calibrated against those measured by other SOHO instruments and other monitoring spacecraft such as Wind with a difference less than 1% and

a spread less than 3% (e.g., Ipavich et al., 1998), the calibration is not made during the IP shock passage when the shock speed suddenly increases. In such conditions, a saturation effect is expected as mentioned in Sect. 2.2. Actually, the SOHO–ACE difference in Fig. 7 indicates that the measured speed behind the shock is smaller (difference is larger) by the ACE observation than by the SOHO observation. In other words, the saturation effect might underestimate the difference. However, Fig. 8 shows that the spread in $V_{\rm triangle}/V_{\rm SW}$ does not depend very much on the solar wind speed, indicating that higher speed (higher risk of saturation) does not affect the $V_{\rm SW}$ measurement.

Also, the small change in the shape of the distribution between Fig. 7b and Fig. 7c, both Gaussian-like, indicates that saturated cases are already removed in Fig. 7c, because the saturation effect may also deform the distribution asymmetric from the Gaussian-like distribution, as in the ACE case in Fig. 7f. In this respect, the solar wind speed (actually energy) of the SOHO measurement after the shock is reliable if we take the largest value within 15 min.

4.2 Change of speeds from L1 to the Earth

It is possible that an IP shock propagation is decelerated while the solar wind is accelerated, like the high-speed CME near the Sun (Yashiro et al., 2004). If the speed changes, we have to correct the solar wind speed to the average speed between L1 and the Earth, because the shock propagation speed is derived as an average value from start-end timings in this paper. Although the velocity measurements are statistically consistent between the L1 monitoring spacecraft and the Earth orbiting spacecraft (e.g., Ipavich et al., 1998), the same argument as above applies here (i.e., measurements near the IP shocks can be different from relatively constant solar wind). If such acceleration is substantial, the real offset in $V_{\rm timing}/V_{\rm SW}$ (and Δt) would be smaller than the present result. However, the distance from L1 to the Earth is only 1% of the distance from the Sun to the Earth. We are not aware of any quantitative model that predicts substantial acceleration of the solar wind (or substantial deceleration of the IP shock) within such a short distance. Therefore, this is again less likely cause error in our results of 7% difference between $V_{\rm triangle}$ and $V_{\rm SW}$.

4.3 Transit time from the magnetopause to the Earth

The onset timing of the geomagnetic SC was used as the proxy of the timing when the IP shock passing the Earth's terminator. Considering about 10^5 km distance from the magnetopause to the Earth, the travelling time of the IP shock (speed of about 400-900 km/s as shown in Fig. 8) to the terminator is estimated about 1-3 min. On the other hand, the effect of the enhanced magnetopause current propagates to the Earth (to cause the geomagnetic SC) with about magnetosonic speed (not the speed of light), resulting in the similar travel time of 1-3 min. Therefore, the resultant uncertainty in Δt should be, if any, only 1-2 min.

If we are to improve the accuracy of Δt, we need to monitor the shock arrival at the magnetopause. The Smile satellite (Wang et al., 2025), recently launched in May 2026, monitors the magnetosheath solar wind with 0.5-2 sec resolution, which is 20 times better than SOHO (Dai et al., 2025), at nearly the same location (apogee) for more than 40 hours out of the nearly 2-day orbit. In addition, Smile can monitor the magnetopause compression using soft X-ray imaging (Sambay et al., 2025). Although the instrument design is 5-min resolution, this can go down to a few minutes for the arrival timing of the strong IP shocks. Then, we may still have a better accuracy of Δt if we have many IP shocks.

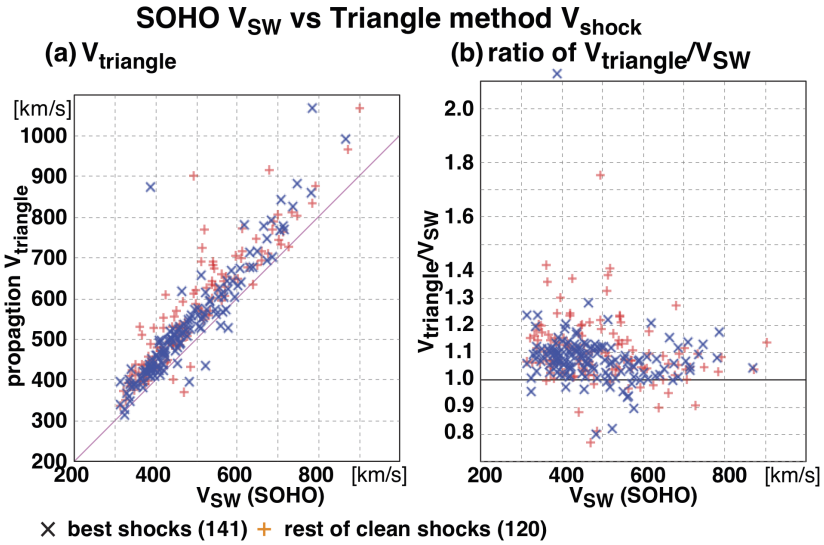

Figure 8. (a) Scatter plot of the shock propagation speed $V_{\rm triangle}$ against the post-shock solar wind speed observed by SOHO for the clean 261 IP shocks, where $V_{\rm triangle}$ is estimated according to Eqs. (3) and (4) (corresponding to Fig. 6b). (b) The same as (a) but for the speed ratio $V_{\rm triangle}/V_{\rm SW}$ (corresponding to Fig. 7b). Best 141 examples are marked by different symbols from the rest of clean examples.

4.4 Tilt of the shock front in the ζ direction

Using the triangle method (Eq. (3)), we could estimate the tilt angle in the η direction (θ_η by the triangle method) with a small uncertainty, as shown in Fig. 3d. However, the estimated tilt angle in the ζ direction (we have only $\theta_{\zeta 1D}$ by the 1D-model method) has a large error range because of a finite uncertainty in the solar wind defection angle (resultant uncertainty in the η–ζ components of the solar wind is not less than 20 km/s). Although the resultant estimation error in the $V_{\rm triangle}/V_{\rm SW}$ value should be equally distributed on both positive and negative sides, shape of the distribution is affected (longer tail toward higher values) as discussed in Sect. 4.1, causing a small effect even in the average value, as is seen from the decreasing average values with more filtering in Figs. 5, 6, and 7.

To minimize the influence by the large uncertainty in $\theta_{\zeta 1D}$, we used the estimated angles θ_η and $\theta_{\zeta 1D}$ just for selecting the IP shocks of which the shock normal points nearly toward the $-X_{\rm GSE}$ direction, such that the error caused by finite θ becomes relatively small. We defined the present criterion (Fig. 3b and Table 1) to keep total numbers of samples statistical liable. The success of the filtering is seen in Fig. 7a-c, where the distribution became more compact and symmetric after more selection. The difference in the scatter plot between the best cases and the rest of the clean cases in Fig. 8 is already small compared to the spread. Therefore, the average difference in the speed (7%) would not decrease more than 1% if a larger dataset allows us to tighten the criterion.

5 Summary and Discussion

We examined IP shocks that have consistent velocity profiles between SOHO and ACE data during 1998-2022. To remove IP shocks with shock surface largely tilted from the $Y_{\rm GSE}$–$Z_{\rm GSE}$ direction, we estimated the tilt angle in the $X_{\rm GSE}$–η–ζ coordinate in Fig. 2, where the η is parallel to the projected two-spacecraft alignment direction on the $Y_{\rm GSE}$–$Z_{\rm GSE}$ plane. In this coordinate, the tilt angle in the η direction (θ_η) is estimated by the triangle method (Eq. (3). For the ζ direction, we used the change in the deflection angle in the ζ direction across the shock, which is more close to the raw data than the estimate $\theta_{\zeta 1D}$ by the simple 1D shock model (Eq. (A2)). The criterions of selecting IP shocks propagating nearly along the $-X_{\rm GSE}$ directions (the clean shocks and the best shocks) are given in Fig. 3b and Table 1.

Statistics of the IP shock during 1998-2022 shows that the geomagnetic SC takes place generally earlier than the predicted solar wind arrival time using the measured solar wind speed at L1 (even using the highest proton speed within 15 min after the IP shock passage). Thus, as is expected from the shock theory, the IP shocks observed by SOHO and ACE propagate to the Earth faster than the solar wind.

For the 141 "best" IP shocks propagating nearly along the $-X_{\rm GSE}$ direction, the time difference Δt (positive value for earlier geomagnetic SC) spreads over -1 to $+10$ min (central 80% range) for SOHO and $+2$ to $+8$ min for SOHO, with a finite number of IP shocks (8 shocks for SOHO and 5 shocks for ACE out of 141 samples) arrived more than 10 min earlier than the predicted solar wind arrival time as shown in Figs. 5c and 5f. The corresponding propagation speed of the IP shock derived by the triangle method (Eq. (4)) for the best 141 shocks is 7% faster than the solar wind speed for SOHO (10% for ACE), with individual $V_{\rm triangle}/V_{\rm SW}$ values ranging from 0% to $+14$% ($+3$ to $+17$% for ACE), as shown in Figs. 7c and 7f. If the propagation speed ($V_{\rm timing}$) is estimated from the timing and $X_{\rm SGE}$ distance of the spacecraft, the distribution is more widespread and more asymmetric from the Gaussian-like distribution for SOHO, as shown in Fig. 6c.

Let us compare the average differences between the IP propagation speed and the solar wind speed (about 7%) with the simple 1D shock model (Eq. (A1) in Appendix A). Here one must note that the model requires density and normal velocity to the shock of both before and after the shock passage (four measured values) instead of only post-shock speed (one measured value) for $V_{\rm triangle}$, and that the resultant shock propagation speed $V_{\rm 1D}$ is very sensitive to the density ratio between before and after the shock, particularly when the ratio is near unity, as shown in Fig. A1e in Appendix A2. Considering that the post-shock density values can be underestimated due to possible saturation of the instrument (cf. Sect. 2.2), the calculated $V_{\rm 1D}$ can be significantly overestimated when the density ratio is close to unity. This effect is seen in the sparse spread of $V_{\rm 1D}/V_{\rm SW}$ values in Fig. A2 in Appendix A (this is why we show this figure in Appendix rather than in the main text).

Removing these overestimated cases, Fig. A2 indicates that a simple 1D model has the dense cluster of $V_{\rm 1D}/V_{\rm SW}$ around $+10$%, which is consistent with the observed speed ($V_{\rm triangle}/V_{\rm SW}$), although individual cases are not well correlated. This indicates that the simple 1D model is a good guide in estimating the shock propagation speed near the Earth, encouraging development of the solar wind measurement method (both density and deflection angle), particularly right after the shock, as well as placing three or more spacecraft near the L1 region.

If only one spacecraft is used, the spread of Δt is as wide as Fig. 1 (and Fig. 5a) due to the oblique shock front (cf. Figs. 2c and 5g), with a substantial fraction arriving > 10 min earlier than the predicted time. This means that one must be ready for possible space weather hazard starting earlier than the predicted arrival time based on the real-time L1 monitor, although one can expect, in average, the shock propagation about 1.1 times faster than the observed solar wind speed. This fact also warns the usage of 1-min resolution solar wind OMNI data at the magnetopause (https://omniweb.gsfc.nasa.gov/), in which the same propagation speed as the measured solar wind speed is used when projecting the L1 observation to the magnetopause nose (Omniweb, 2026).

6 Conclusions

As is expected from the shock theory, the IP shocks observed by SOHO and ACE propagate to the Earth faster than the solar wind. We used two spacecraft instead of one to select nearly radially propagating IP shocks (shock normal is not tilted very much from the $-X_{\rm GSE}$ direction) through two selecting parameters (equivalent to the shock angle in two directions) to as shown in Figs. 2c and 3b. For the best 141 shock that are selected in this manner, the shock propagate faster than solar wind speed measure by SOHO (maximum value within 15 min after the shock) by about 7% in average with standard deviation of 9% (average 10% with standard deviation of 7% for ACE).

The shock tilt angle that is estimated by simple 1D shock model using velocity change across the shock of ACE gives, although this method has large instrumental uncertainty, generally consistent value with what is estimated by the triangle method in the spacecraft alignment direction within that large uncertainty. The same applies even for the propagation speed, although the 1D-model method has even larger instrumental uncertainty.

Data availability. SOHO data is taken from SOHO site (https://l1.umd.edu/) and NASA NASADCC site (https://cdaweb.gsfc.nasa.gov/). ACE data is taken from both ACE site (https://izw1.caltech.edu/ACE/ASC/level2/index.html) and NASA NASADCC site (https://cdaweb.gsfc.nasa.gov/). Geomagnetic indices are taken WDC-C2 for geomagnetism, Kyoto University (https://wdc.kugi.kyoto-u.ac.jp/wdc/Sec3.html). Another list of geomagnetic sudden commencement is found at Ebre Observatory data portal (https://www.obsebre.es/en/variations/rapid).

Appendix A: 1D-shock mass flux conservation relation

Fig. A1 illustrates the mass flux conservation relation for a textbook-type 1D shock. Through conservation relation in the shock frame, the density n and velocity normal to the shock v in the spacecraft frame has a relation of

$$n_a \cdot (V_{\rm 1D} - v_a) = n_b \cdot (V_{\rm 1D} - v_b)$$

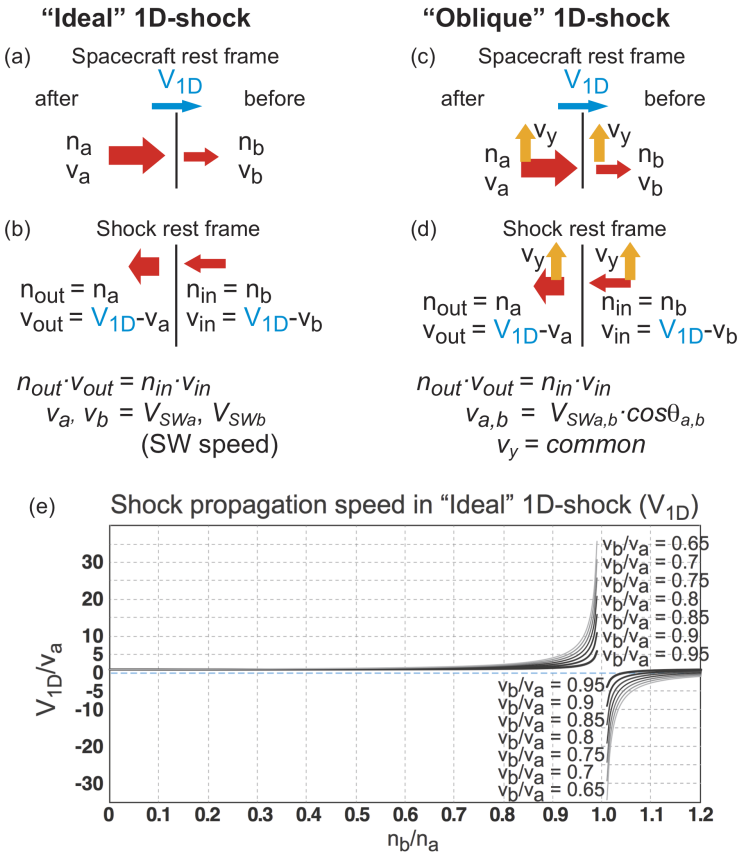

Figure A1. (a) and (b) Illustration of mass flux ($n \cdot v$, where n is density and v is 1D speed) conservation across the simplest 1D shock in (a) spacecraft rest frame and (b) shock rest frame. (c) and (d) A more general 1D shock case with finite flow velocity along the shock surface. To distinguish this direction from GSE ($Y_{\rm GSE}$) or spacecraft alignment coordinate (η) in Fig. 2, we use small y to denote this direction. (e) Theoretical values $V_{\rm 1D}/v_a$ (ratio between the shock propagation speed $V_{\rm 1D}$ and the flow speed after the shock v_a) is plotted against n_b/n_a (inverse of the shock compression ratio) for different velocity changes. Suffix "a", "b", and "1D" in the upper panel denote after the shock passage, before the shock passage, and shock front, respectively. Suffix "in" and "out" in the lower panel denote the inflow to the shock and outflow from the shock, respectively.

405 or

$$(V_{\rm 1D}/v_a) = \frac{1-\epsilon\cdot(v_b/v_a)}{(1-\epsilon)} \qquad \text{(A1)}$$
$$> 1 \ \ (\text{for forward shock})$$

where $\epsilon = (n_b/n_a) < 1$ is inverse of the shock compression ratio, and suffix "a", "b", and "1D" denote after the shock passage, before after the shock passage, and shock front, respectively.

A1 1D-model shock angle $\theta_{\eta 1D}$ and $\theta_{\zeta 1D}$

This relation is unchanged when the flow component along the shock front (v_y) is added (cf. Figs. A1c and A1d), as long as v_y is the same between the upstream and downstream (i.e., no vorticity is carried by the shock, which is normally the case for high Alfvén Mach number shocks). In this case, the shock normal direction $\overrightarrow{\mathbf{n}}$ is approximately

$$\overrightarrow{\mathbf{n}} \sim (dv_X, dv_\eta, dv_\zeta)/|dv| \tag{A2}$$

where $d\overrightarrow{\mathbf{v}} = (dv_X, dv_\eta, dv_\zeta)$ is the change in the solar wind velocity across the shock in the spacecraft frame, and θ is the shock angle (e.g., Paschmann and Daly (1999) Eq. (10.18)). In the present paper, we use $\tan\theta_{\zeta 1D} = +dV_\zeta/dV_X$ and $\tan\theta_{\eta 1D} = +dV_\eta/dV_X$ in Eq. (A2) (propagation direction toward $-X_{\rm GSE}$ determines the sign in the present definition of θ_η and $\theta_{\zeta 1D}$) when comparing with the triangle method in Sect. 2.2.

The propagation speed in the shock normal direction $\mathbf{V}_{1D}$ is approximately

$$(V_{\rm 1D}/v_a) \sim \frac{1-\epsilon\cdot(v_b/v_a)}{(1-\epsilon)}\cdot\cos\theta \tag{A3}$$

where θ is the shock angle (e.g., Paschmann and Daly (1999) Eq. (10.29)), while the earthward phase velocity becomes the same as Eq. (A1).

A2 Density underestimation effect in deriving the propagation speed

Although Eq. (A1) provides $V_{\rm 1D}/v_a$, one cannot simply trust the derived values in the actual shock observations because of the high uncertainty in the solar wind measurement (particularly density) right after the shock: n_a (and possibly v_a) can be significantly underestimated due to saturation of the ion instrument, as explained in Sect. 2.2. This makes overestimation of the n_b/n_a values for some shocks, making them much closer values to unity than it actually is. As shown in Fig. A1e, the $V_{\rm 1D}/v_a$ value is very sensitive to n_b/n_a value near $n_b/n_a = 1$, making small underestimation of n_a resulting in large overestimation of $V_{\rm 1D}$ (and $V_{\rm 1D}/V_{\rm SW}$). This is why we did not show the distribution plots of $V_{\rm 1D}/V_{\rm SW}$.

Fig. A2 shows scatter plots comparing theoretical 1D shock speed $V_{\rm 1D}$ using density and velocity values of SOHO both before and after the shock (according to Eq. (A1)) and measured $V_{\rm triangle}$ between L1 and Earth based on Eq. (4). Since the density is more variable than the velocity, we took average values over 10 min periods for the solar wind values in Fig. A2: 3-13 min before the shock and 3-13 min after the shock. Nevertheless, there are several cases when the density values superficially decreased after the shock even it is forward shock according to the ACE data. We removed such obvious cases of unreliable density data as well as the reverse shocks in Fig. A2. After normalized by $V_{\rm SW}$ (Fig. A2b), values of $V_{\rm triangle}/V_{\rm SW}$ and $V_{\rm 1D}/V_{\rm SW}$ fall into the same range (majority around $+10\%$) although individual cases are not well correlated to each other.

We also examined the effect of tilt angle (η and particularly ζ) by subdividing the dataset into the best examples and rest of the clean examples (i.e., larger angle than the best examples). After removing obviously overestimated cases, no outstanding difference is seen between them. As is already seen in Fig. 7, selecting the best cases makes the distribution in the horizontal direction more compact than all clean cases, but not in the vertical axis ($V_{\rm 1D}/V_{\rm SW}$).

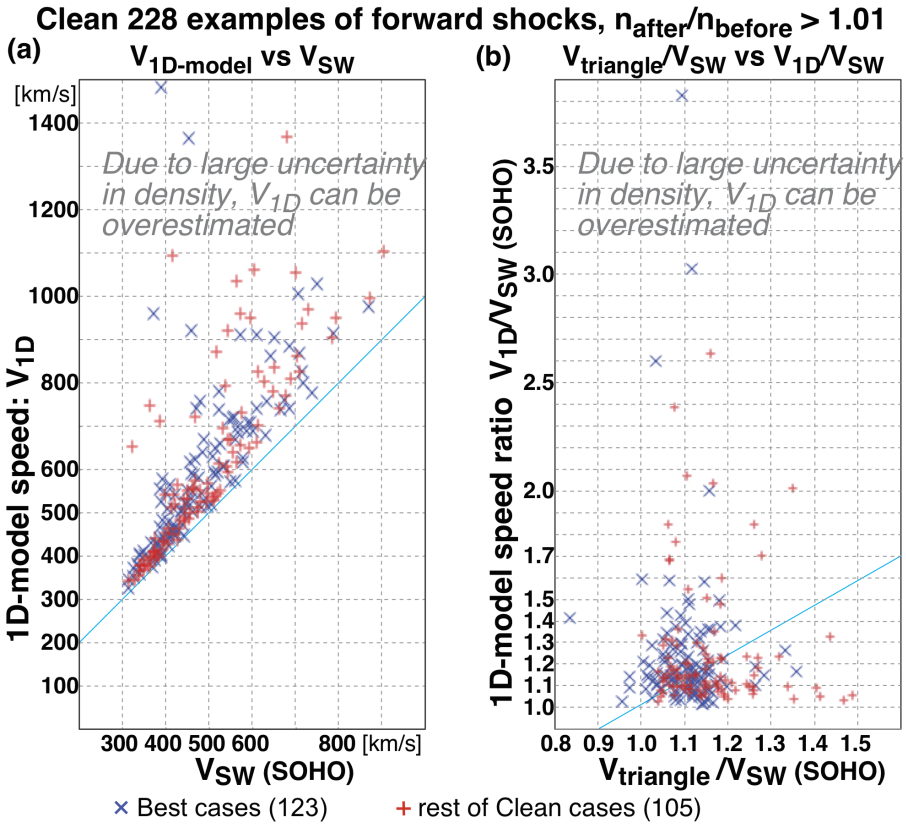

Figure B1. Scatter plot of 228 clean examples of forward shocks (selected from the 261 clean shocks) between V_{1D} according to Eq. (A1) and velocity values of SOHO both before and after the shock) and the measured $V_{triangle}$ according to Eq. (4): (a) V_{1D} against V_{SW}; (b) V_{1D}/V_{SW} against $V_{triangle}/V_{SW}$ (comparing the normalized speed. The solar wind values used in these specific plots are 10 min average values over 3-13 min before the shock and 3-13 min after the shock. Different symbols mean the different dataset defined by Table 1. We further limited the dataset to those with clear forward shock and with clear geomagnetic SC signature (seen two different methods).

Appendix C: Conversion from Y_{GSE}-Z_{GSE} coordinate to η–ζ coordinate

Fig. 2a shows the η–ζ coordinate system that is tilted by angle ϕ from the Y_{GSE}–Z_{GSE} coordinate system, where ϕ is the SOHO-ACE alignment direction in the Y_{GSE}–Z_{GSE} plane. After a rotation by ϕ, a coordinate (Y_{GSE}, Z_{GSE}) and a vector (v_Y, v_Z) are expressed in the η–ζ coordinate as

$$\eta = Y_{GSE}\cos\phi + Z_{GSE}\sin\phi$$

$$\zeta = Z_{GSE}\cos\phi - Y_{GSE}\sin\phi$$

$$v_\eta = v_Y\cos\phi + v_Z\sin\phi$$

$$v_\zeta = v_Z\cos\phi - v_Y\sin\phi$$

In the configuration of Fig. 2a, the η axis is parallel to the alignment between (Y_1, Z_1) and (Y_2, Z_2) in the $Y_{\rm GSE}$–$Z_{\rm GSE}$ plane with distance $D = \zeta_1 = \zeta_2$. Therefore, we have a relation

$$\begin{aligned}
\cos\phi &= (Y_2 - Y_1)/r \\
\sin\phi &= (Z_2 - Z_1)/r \\
r &= \sqrt{(Y_2 - Y_1)^2 + (Z_2 - Z_1))^2} \\
D &= (Z_1 \cdot Y_2 - Y_1 \cdot Z_2)/r
\end{aligned} \tag{C1}$$

and final conversion formulae

$$\begin{aligned}
\eta &= Y \cdot (Y_2 - Y_1)/r + Z \cdot (Z_2 - Z_1)/r \\
\zeta &= Z \cdot (Y_2 - Y_1)/r - Y \cdot (Z_2 - Z_1)/r \\
v_\eta &= v_Y \cdot (Y_2 - Y_1)/r + v_Z \cdot (Z_2 - Z_1)/r \\
v_\zeta &= v_Z \cdot (Y_2 - Y_1)/r - v_Y \cdot (Z_2 - Z_1)/r
\end{aligned} \tag{C2}$$

Appendix D: Timing list of IP shocks

Table A1 lists the timings of the best 141 IP shocks (see Table 1) that are used in the statistical study. The second and third columns show the UT of IP shock detection by SOHO and by ACE, respectively. The fourth column shows the onset UT of sudden increase of SYM-H. The last column indicates the clearness of the SC (see caption of Fig. 1).

In the same format, Table A2 lists the timings of the remaining 120 IP shocks other than the best 141 shocks (after removing the samples listed in Table A1) out of 261 "clean" IP shock in Table 1.

Similarly, Table A3 lists the timings of the remaining 114 IP shocks (after removing the samples listed in Tables A1 and A2) out of 375 "consistent" IP shock on Table 1.

Finally, Table A4 lists the timings of the 63 IP shocks with only SOHO data (after removing the samples listed in Tables A1–A3) out of 438 "basic samples" IP shock in Table 1.

Author contributions. MY and YY initiated the work. YY made overview plots related to SOHO and ACE in several format for all the events, and prepared tables that contain the velocity, timing, and the expected transit time. MY made the sub-dataset of the geomagnetic SYM-H indices (SYMASY) to identify the onset timing of geomagnetic SC timing, and examined all these plots to revise and complete the table made by YY. TK mainly contributed to SYM-H part, and JM made independent SC list from different dataset. MY made first draft of the text and figures, while all others contributed the text and discussion.

Competing interests. The authors declare that they have no competing interests.

Acknowledgements. SOHO is a project of international cooperation between ESA and NASA. ACE is a NASA project that is aimed as the solar wind monitor during the International Solar Terrestrial Program. Data from both spacecraft are open access. The authors gratefully thank the instrument teams that maintained the quality of the solar wind data at L1 for nearly 30 years that are used in this study: SOHO PM team (PI: F.M. Ipavich), ACE SWEPAN team (PI: D.J McComas), and ACE MG team (PI: N. Ness). The NASA OMINI data at Omniweb site (https://cdaweb.gsfc.nasa.gov/) is maintained by Space Physics Data Facility, NASA Goddard Space Flight Center.

Geomagnetic indices SYMASY and AE are calculated by World Data Center (WDC) for Geomagnetism, Kyoto using geomagnetic field data at SYMASY stations (San Juan, Fredericksburg, Boulder, Tucson, Papeete, Honolulu, Memambetsu, Urumqi, Alma Ata, Alibag, Martin de Vivies, Hermanus, Chambon-la-Foret) and AE stations (Abisko, Amderma, Dixon Island, Cape Chelyuskin, Tixie Bay, Pebek, Cape Wellen, Barrow, College, Yellowknife, Fort Churchill, Sanikiluaq, Great Whale River, Poste-de-la-Baleine, Narsarsuaq, Leirvogur). The geomagnetic SC list at Ebre Observatory (https://www.obsebre.es/en/variations/rapid) is derived from geomagnetic field data at many stations listed there. We thank all these contributing observatories.

Special thank goes to T. Araki (deceased August 2025) who initiate another work for which the produced plots lead this work. Without him, we never started this work. MY is partly supported by Swedish National Space Agency (dnr 2024-00124).

References

Araki, T.: Global structure of geomagnetic sudden commencements, Planet. Space Sc., 25, 373?384, https://doi.org/10.1016/0032-0633(77)90053-8, 1977.

Araki, T.: A Physical Model of the Geomagnetic Sudden Commencement, 183-200, American Geophysical Union (AGU), ISBN 9781118663943, https://doi.org/10.1029/GM081p0183, 1994.

Collier, M.R., Slavin, J.A.,, Lepping, R.P., Szabo, A., and Ogilvie, K.: Timing accuracy for the simple planar propagation of magnetic field structures in the solar wind, Geophys. Res. Lett., 25, 2509-2512, https://doi.org/10.1029/98GL00735, 1998.

Dai, L., Kong, L., Zhang, A. Kataria, D., Berthomier, M., et al.: The light ion analyzer (LIA) for the SMILE mission, Space Sci. Rev., 221, 109, https://doi.org/10.1007/s11214-025-01235-w, 2025

Gonzalez-Esparza, A. and Aguilar-Rodriguez, E.: Speed evolution of fast CME/shocks with SOHO/LASCO, WIND/WAVES, IPS and in-situ WIND data: analysis of kilometric type-II emissions, Ann. Geophys., 27, 3957–3966, https://doi.org/10.5194/angeo-27-3957-2009, 2009.

Gopalswamy, N., Yashiro, S., Michalek, G., Stenborg, G., Vourlidas, A., Freeland, S., and R. Howard, R.: The SOHO/LASCO CME Catalog, Earth, Moon, Planet., 104, 295-313 https://doi.org/10.1007/s11038-008-9282-7, 2009.

Ipavich, F.M., Galvin, A.B., Lasley, S.E., Paquette, J.A., Hefti, S., Reiche, K.U., et al.: Solar wind measurements with SOHO: The CELIAS/MTOF proton monitor J. Geophys. Res., 103, 17205-17213 https://doi.org/10.1029/97JA02770, 1998.

King, J., and Papitashvili, N.: Explanation of one min and 5-min solar wind data sets at the Earth's bow shock nose of OMNIWeb, https://omniweb.gsfc.nasa.gov/html/omni_min_data.html#3, (last access, 12 February 2026), 2025.

Manoharan, P.K., Tokumaru, M., Pick, M., Subramanian, P., Ipavich, F.M., Schenk, K., Kaiser, M.L., Lepping, R.P., and Vourlidas. A.: Coronal mass ejection of 2000 July 14 flare event: Imaging from near-Sun to Earth environment, Astrophys. J., 559, 1180-1189, https://doi.org/10.1086/322332, 2001.

McComas, D.J., Bame, S.J., Barker, P., Feldman, W.C., Phillips, J.L., Riley, P., and J.W. Griffee J.W.: Solar Wind Electron Proton Alpha Monitor (SWEPAM) for the Advanced Composition Explorer, Space Sci. Rev. 86, 563–612, https://doi.org/10.1023/A:1005040232597, 1998.

Milan, S.E., Carter, J.A., Bower, G.E., Fleetham, A.L., and Anderson, B.J.: Influence of off-Sun-Earth line distance on the accuracy of L1 solar wind monitoring, J. Geophys. Res., 127, e2021JA030212, https://doi.org/10.1029/2021JA030212, 2022

Nanjo, S., Yamauchi, M., Johnsen, M.G., Yokoyama, Y., Brändström, U., Ogawa, Y., Willer, A.N., and Hosokawa, K.: Leaping and vortex motion of the shock aurora toward the late evening sector observed on 26 February 2023, Ann. Geophys., 43, 303-317, https://doi.org/10.5194/angeo-43-303-2025, 2025.

NASA Goddard Space Flight Center: Omniweb Plus https://omniweb.gsfc.nasa.gov/, (last access, 16 June 2026), 2026.

Ogilvie, K.W., Chornay, D.J., Fritzenreiter, R.J., Hunsaker, F., Keller, J., et al.: SWE, a comprehensive plasma instrument for the WIND spacecraft, Space Sci. Rev., 71, 55-77, https://doi.org/10.1007/BF00751326, 1995.

Paschmann, G. and Daly, P. W. (editors): Analysis Methods for Multi-Spacecraft Data, ISSI Scientific Reports, ESA Publ. Div., Noordwijk, Netherlands, http://www.issibern.ch/PDF-Files/analysismethods11a.pdf, 1999.

Paularena, K.I., Richardson, J.D., Zastenker, G.N., Dalin, P.A.: Solar wind correlations: Using a solar wind monitor successfully, In: Sibeck, D.G., Kudela, K. (eds) Interball in the ISTP Program. NATO Science Series, vol 537. Springer, Dordrecht. https://doi.org/10.1007/978-94-011-4487-2_12, 1999.

Paularena, K.I., Zastenker, G.N., Lazarus, A.J. and Dalin, P.A.: Solar wind plasma correlations between IMP 8, INTERBALL-1 and WIND, J. Geophys. Res., 103, 14601-14617, https://doi.org/10.1029/98JA00660, 1998.

Richardson J.D., and Paularena, K.I.: The orientation of plasma structure in the solar wind, Geophys. Res. Lett., 25, 2097-2100, https://doi.org/10.1029/98GL01520, 1998.

Sembay, S., Cheney, A., Hampson, R., et al.: The soft X-ray imager (SXI) on the SMILE Mission, Space Sci. Rev. 221, 113, https://doi.org/10.1007/s11214-025-01241-y, 2025.

Tokumaru, M., Kojima, M., Fujiki, K., and Yamashita, M.: Tracking heliospheric disturbances by interplanetary scintillation, Nonlin. Processes Geophys., 13, 329–338, https://doi.org/10.5194/npg-13-329-2006, 2006.

Toth, G., Dredger, P., and Pulkkinen, T.: Michigan geospace model with ensemble forecasting and particle filtering: Modeling the May 2024 extreme storm, Space Weather, 24, e2026SW005083, https://doi.org/10.1029/2026SW005083, 2026.

Wang, C., Branduardi-Raymont, G., Escoubet, C.P., and Forsyth, C.: Solar wind magnetosphere ionosphere link explorer (SMILE): Science and mission overview, Space Sci. Rev. 221, 9, https://doi.org/10.1007/s11214-024-01126-6, 2025.

Yashiro, S., Gopalswamy, N., Michalek, G., St. Cyr, O.C., Plunkett, S.P., Rich, N.B., and Howard, R. A.: A catalog of white light coronal mass ejections observed by the SOHO spacecraft, J. Geophys. Res., 109, A07105, https://doi.org/10.1029/2003JA010282, 2004.

Table A1: Timing of IP detection and geomagnetic SC for best 141 samples

date	**SOHO**	**ACE**	**SYM-H**	**SC**[*1]
19980501	21:14	21:22	21:57	2
19981107	07:34	07:37	08:16	2
19990310	00:45	00:40	01:31	2
19990517	23:53	24:03	24:57	2
19990626	19:27	19:25	20:17	2
19990804	01:30	01:16	02:20	2
19990815	09:51	09:38	10:44	2
19991028	11:16	11:27	12:16	2
20000111	13:51	13:40	14:27	2
20000211	02:21	02:13	02:59	2
20000604	14:17	14:23	15:02	2
20000608	08:42	08:42	09:10	2
20000713	09:10	09:01	09:43	2
20000726	18:08	17:55	18:57	2
20000728	05:53	05:42	06:34	2
20000906	16:18	16:13	17:01	2
20001002	23:58	24:08	24:54	2
20001005	02:35	02:40	03:26	2
20001012	21:35	21:44	22:28	2
20001028	09:00	09:08	09:55	2
20001126	11:25	11:23	11:58	2
20010110	15:28	15:19	16:21	2
20010117	15:45	15:31	16:32	2
20010123	10:15	10:06	10:49	2
20010319	10:12	10:22	11:14	2
20010322	12:32	12:42	13:42	2
20010527	14:17	14:18	14:59	2
20010618	01:53	01:55	03:00	2
20010803	06:37	06:25	07:16	2
20010817	10:26	10:16	11:03	2
20010929	09:03	09:05	09:39	2
20010930	18:41	18:46	19:25	2
20011011	16:12	16:20	17:01	2
20011115	13:45	13:53	15:09	2
20011119	17:35	17:35	18:15	2
20011229	04:56	04:47	05:38	2
20011230	19:39	19:32	20:10	2
20020318	12:32	12:36	13:21	2
20020329	21:27	21:40	22:37	2
20020423	04:07	04:15	04:49	2
20020510	02:40	10:29	11:24	2
20020511	09:16	09:25	10:14	2
20020520	02:57	02:57	03:41	2
20020725	13:03	12:59	13:37	2
20020930	07:13	07:21	08:16	2
20021109	17:56	17:55	18:50	2
20030408	00:04	00:15	01:12	2
20030529	11:53	11:52	12:25	2
20030817	13:38	13:41	14:22	2
20031024	14:47	14:48	15:25	2
20031104	05:53	05:58	06:26	2
20040122	01:10	01:04	01:36	2
20040403	08:49	08:56	09:48	2
20040409	01:47	01:49	02:33	2
20040726	22:28	22:26	22:49	2
20040730	20:41	20:31	21:14	2
20040913	19:29	19:34	20:02	2
20041107	17:59	17:53	18:27	2
20050121	16:49	16:47	17:11	2
20050528	03:47	03:31	04:37	2
20050529[*3]	09:15	09:03	09:53	2
20050710	02:56	02:47	03:38	2
20050727	18:43	18:49	19:39	2
20050915	08:25	08:29	09:05	2
20060428	00:20	00:11	01:18	2
20070927	10:53	10:54	11:52	2
20071217	02:02	02:04	02:53	2
20080528	01:32	01:28	02:25	2
20090303	04:53	04:51	06:03	2
20091004[*3]	03:15	03:07	04:14	2
20100405	07:59	07:54	08:27	2
20100803	16:51	16:55	17:41	2
20110909	11:49	11:42	12:43	2
20110917	03:05	02:55	03:44	2
20111005	06:55	06:46	07:37	2
20111024	17:50	17:48	18:31	2
20120423	02:29	02:27	03:21	2
20120616	08:52	08:57	09:56	2
20120616	19:24	19:30	20:20	2
20120616	20:30	20:31	21:16	2
20120903	11:33	11:22	12:14	2
20120930	22:21	22:13	23:07	2
20121031	14:46	14:39	15:40	2
20130125	16:04	16:00	17:00	2
20130216	11:12	11:10	12:10	2
20130518[*3]	00:24	00:23	01:11	2
20130627	13:45	13:52	14:39	2
20130820	21:43	21:33	22:29	2
20131002	01:24	01:18	01:56	2
20131213	12:01	12:08	13:24	2
20140623	22:01	22:01	23:08	2
20140714	13:28	13:30	14:32	2
20140911	23:02	22:57	23:45	2
20141221	18:22	18:23	19:12	2
20150506	00:50	00:53	01:43	2
20150622	04:52	04:51	05:45	2
20150815	07:49	07:44	08:30	2
20150920	05:32	05:27	06:05	2
20151106	17:32	17:34	18:19	2
20151219	15:27	15:28	16:17	2
20161012	21:25	21:19	22:13	2
20161109[*3]	05:28	05:34	06:44	2
20170716	05:18	05:17	06:00	2
20170831	04:49	04:44	05:39	2
20170906	23:13	23:08	23:45	2
20170914	10:20	10:19	11:16	2
20180108	05:59	05:52	06:47	2

20190510	16:50	16:53	17:55	2
20190924	12:00	12:03	13:11	2
20201210	01:33	01:33	02:10	2
20210512	05:45	05:49	06:39	2
20210827	00:28	00:24	01:16	2
20211127	22:06	21:59	22:52	2
20211227	08:51	08:41	09:37	2
19990815	18:47	18:35	19:38	1
20000711	08:22	08:17	09:16	1
20010818	05:37	05:24	06:14	1
20020110	15:52	15:44	16:20	1
20020322	03:23	03:23	04:07	1
20021002	22:08	22:14	22:55	1
20060818*3	15:41	15:49	16:42	1
20071112	21:37	21:26	22:21	1
20090114	00:05	00:13	01:20	1
20090624	09:45	09:51	11:02	1
20110929	00:27	00:20	01:04	1
20130525	09:06	09:09	09:49	1
20151104	03:23	03:23	03:54	1
20220723	02:30	02:26	02:58	1
19980218*3	08:01	07:53	08:44	?
19981108	04:19	04:21	04:52	?
19990228	20:46	20:33	21:32	?
19990823	11:38	11:29	12:24	?
20001028	05:31	05:41	06:40	?
20010830	13:26	13:30	14:12	?
20021219	13:31	13:17	14:22	?
20030529	18:36	18:30	19:01	?
20030717*2	00:13	00:08	00:42	?
20041205	04:16	04:06	05:11	?
20141228*2	22:02	22:08	22:57	?
20170716	16:58	16:53	17:39	?
20171217	06:36	06:33	07:24	?

1: Identification of geomagnetic SC by both methods (=2), by only SYM-H (=1), and weak/unclear SC (=?)
*2: Reverse shock
*3: Density measurement is skeptical.

Table A2 Timing of IP detection and geomagnetic SC for better 120 samples

date	**SOHO**	**ACE**	**SYM-H**	**SC**
19980407	16:58	16:51	17:51	2
19980423	17:13	17:28	18:25	2
19980515	13:41	13:57	14:52	2
19980529	14:58	15:03	15:38	2
19990626	02:35	02:18	03:25	2
19990702	00:22	00:24	01:00	2
19990706	14:22	14:17	15:10	2
19990712	01:09	01:15	02:20	2
19991021	01:33	01:38	02:26	2
19991105	19:07	19:14	20:10	2
20000211	23:23	23:18	23:53	2
20000220	20:56	20:46	21:40	2
20000406	16:01	16:04	16:40	2
20000710	05:55	05:57	06:39	2
20001031	16:22	16:30	17:15	2
20001128	04:47	04:57	05:31	2
20010303	10:52	10:40	11:22	2
20010404	14:20	14:22	14:54	2
20010408	10:23	10:32	11:02	2
20010417	23:56	00:05	24:47	2
20010421	14:57	15:06	16:01	2
20010812	10:49	10:49	11:35	2
20010914	01:07	01:18	02:05	2
20011021	16:05	16:12	16:47	2
20011031	12:49	12:53	13:49	2
20020131	20:44	20:38	21:26	2
20020228	03:49	04:03	04:51	2
20020323	10:46	10:53	11:36	2
20020417	10:13	10:21	11:07	2
20020419	07:58	08:02	08:35	2
20020518	19:29	19:19	20:08	2
20020530	01:25	01:32	02:05	2
20020729	12:43	12:40	13:22	2
20020818	18:15	18:10	18:46	2
20021126	21:21	21:10	21:51	2
20031026	18:35	18:31	19:09	2
20031115	05:27	05:18	05:50	2
20031120	07:29	07:28	08:03	2
20040829	09:20	09:17	10:06	2
20041205	07:04	06:55	07:47	2
20050824	05:33	05:38	06:13	2
20060101	13:35	13:30	14:05	2
20061214	13:56	13:52	14:15	2
20071025	10:56	10:38	11:35	2
20080624	19:08	19:18	20:11	2
20081124	22:47	22:48	23:52	2
20090528	04:21	04:16	05:20	2
20090903	14:54	14:46	15:53	2
20100402	06:45	06:35	07:16	2
20100411	12:18	12:13	13:04	2
20110214	15:02	14:56	15:57	2
20110218	00:41	00:41	01:31	2

20110329	15:13	15:01	16:03	2
20110418	06:06	05:56	06:52	2
20110711	08:05	08:10	08:50	2
20110805	17:23	17:21	17:51	2
20110926	12:02	11:52	12:35	2
20120122	05:18	05:15	06:12	2
20120226	21:07	20:56	21:40	2
20120307	03:47	03:35	04:20	2
20120312	08:45	08:42	09:15	2
20120315	12:42	12:35	13:08	2
20120521	18:52	18:44	19:38	2
20120714*3	17:27	17:27	18:10	2
20121112	22:08	22:15	23:13	2
20130315	04:46	04:40	05:27	2
20130317	05:34	05:27	06:01	2
20130519	22:13	22:20	23:09	2
20130524	17:40	17:36	18:11	2
20130531	15:32	15:30	16:19	2
20130709	19:58	19:56	20:53	2
20140107	06:30	14:25	15:14	2
20140207	16:28	16:17	17:06	2
20140220	02:58	02:51	03:20	2
20140227	16:17	16:07	16:51	2
20140503	16:51	16:49	17:48	2
20140912	15:27	15:26	15:54	2
20141110	01:31	01:36	02:21	2
20141223	10:30	10:33	11:16	2
20150317	04:10	04:03	04:45	2
20150622	18:01	17:59	18:33	2
20160118	20:52	20:55	21:58	2
20160719	23:09	23:03	23:51	2
20170907	22:38	22:35	23:01	2
20190526	21:01	21:09	22:15	2
20190727	08:12	08:07	09:09	2
20210526	11:53	11:45	12:45	2
20220201	21:42	21:36	22:22	2
20220313	10:09	10:06	10:47	2
20230315	03:42	03:48	04:28	2
20000814	21:48	21:36	22:19	1
20000915	04:14	03:59	04:49	1
20010104	13:07	13:07	14:02	1
20021224	13:18	13:14	13:55	1
20030509	04:49	04:56	05:20	1
20030530	16:02	15:53	16:24	1
20030620	08:04	07:56	08:37	1
20040801	02:02	01:49	02:28	1
20050217	22:00	22:04	22:46	1
20050801	06:09	06:05	06:37	1
20111030	08:56	08:54	10:02	1
20120121*3	03:49	04:00	05:02	1
20120222*2	01:34	01:24	02:16	1
20120520	01:44	01:37	02:15	1
20120904*3	22:12	22:03	22:46	1
20120912	20:17	20:04	21:05	1
20121126	04:32	04:36	05:14	1
20150331*3	07:40	07:41	08:34	1
20200630	01:35	01:23	02:17	1
20220615	04:07	04:00	04:35	1
20000726	03:02	02:53	03:52	?
20000728	09:19	09:09	09:57	?
20050131	09:58	09:50	10:22	?
20110623	02:18	02:24	02:59	?
20140219	03:14	03:09	03:49	?
20140810	21:39	21:26	22:31	?
20150201*3	06:10	06:01	06:39	?
20150223	22:01	21:49	22:47	?
20170520*2	08:50	08:49	09:23	?
20190404	13:06	13:08	14:09	?

*1: Identification of geomagnetic SC by both methods (=2), by only SYM-H (=1), and weak/unclear SC (=?)
*2: Reverse shock
*3: Density measurement is skeptical.

Table A3 Timing of IP detection and geomagnetic SC for very oblique 114 samples

Date	SOHO	ACE	SYM-H	SC[*1]
19980503	17:05	17:00	17:44	2
19980508	09:23	09:21	09:52	2
19980613	18:25	18:55	19:26	2
19990416	10:46	10:35	11:26	2
19990505	14:45	14:59	15:43	2
19990912	03:14	03:20	04:00	2
19991212	15:14	15:14	15:52	2
20000127	14:13	13:56	14:53	2
20000205	15:00	14:48	15:44	2
20000214	07:07	06:56	07:33	2
20000623	12:33	12:27	13:03	2
20000719	15:00	14:47	15:26	2
20000811	18:18	18:11	18:46	2
20001104	01:29	01:34	02:21	2
20001106	09:06	09:15	09:49	2
20010131	07:35	07:22	08:05	2
20010327	17:02	17:15	17:47	2
20010331	00:14	00:23	00:52	2
20010411	13:02	13:14	13:44	2
20010413	07:05	07:13	07:35	2
20010428	04:28	04:31	05:00	2
20010827	19:14	19:19	19:53	2
20011025	07:57	08:02	08:50	2
20011028	02:33	02:43	03:19	2
20020217	01:56	02:09	02:55	2
20020320*3	13:04	13:06	13:28	2
20020523	10:17	10:14	10:50	2
20020717	15:29	15:26	16:03	2
20020719	09:36	09:32	10:09	2
20020801*3	04:44	04:24	05:11	2
20020801	22:30	22:20	23:11	2
20030320	04:21	04:21	04:44	2
20030618	04:44	04:29	05:13	2
20040410	19:26	19:26	20:10	2
20040412	17:34	17:36	18:17	2
20040722	09:45	09:54	10:37	2
20041107	02:22	01:53	02:57	2
20041107	10:22	09:58	10:53	2
20041109	09:05	09:14	09:31	2
20050612	06:58	06:51	07:46	2
20050902	13:32	13:40	14:20	2
20050909	13:10	13:16	14:01	2
20060709*3	21:04	20:46	21:37	2
20060819	10:39	10:50	11:32	2
20061216	17:43	17:22	17:56	2
20070507	07:48	07:25	08:27	2
20070920	09:26	09:05	10:13	2
20091021	23:25	23:07	24:18	2
20110310	05:45	06:08	06:34	2
20110604	19:45	19:58	20:45	2
20110610*3	08:11	08:07	08:48	2
20110617	02:05	02:01	02:40	2
20110804*3	21:10	21:04	21:54	2
20111128	21:27	21:15	21:51	2
20120720	04:00	04:16	04:49	2
20120721	15:25	15:34	16:13	2
20121008	04:31	04:31	05:17	2
20121123	21:22	21:11	21:53	2
20130119	16:34	16:46	17:34	2
20130413	22:24	22:13	22:54	2
20131008	19:51	19:40	20:21	2
20140109	19:33	19:31	20:10	2
20140325	19:23	19:25	20:04	2
20140607	15:57	16:08	16:53	2
20140702	23:33	23:26	24:43	2
20140819	06:14	05:58	06:59	2
20150621	15:50	15:41	16:45	2
20151231	00:10	00:02	00:50	2
20160414	06:45	06:51	07:37	2
20170527	14:27	14:39	15:34	2
20170708	23:27	23:13	24:11	2
20180215	08:06	07:50	08:37	2
20180309	17:17	17:22	18:07	2
20180419	22:59	23:10	24:22	2
20190708	18:38	18:30	19:23	2
19990221	21:52	21:46	22:41	1
20000424	08:53	08:51	09:26	1
20000713	09:32	09:19	09:54	1
20010113	01:50	01:43	02:20	1
20010327	01:03	01:09	01:44	1
20010407	16:44	16:58	17:33	1
20010411	15:18	15:27	15:47	1
20011001	21:15	21:29	22:02	1
20031106	18:56	19:19	19:41	1
20031207	14:01	13:41	14:18	1
20041109	18:24	18:20	18:49	1
20060815	16:26	16:24	17:26	1
20110805	18:32	18:31	19:02	1
20130623	03:53	03:56	04:27	1
20130718	12:49	12:41	13:32	1
20131029	09:25	09:34	10:35	1
20140706	09:51	09:41	11:05	1
20150302	02:47	02:37	03:18	1
20150325	09:21	09:06	09:58	1
20150624	13:01	12:57	13:28	1
20151024	18:39	18:27	18:56	1
20211031	09:34	09:29	10:12	1
19980504	02:36	02:29	02:57	?
19991113	12:04	12:13	12:55	?
20010802	14:27	14:06	15:11	?
20020315	18:00	18:26	19:21	?
20020826	10:19	10:46	11:32	?
20020907	15:53	16:09	16:37	?
20030703	13:16	13:09	13:53	?
20030727*2	04:42	04:38	05:16	?
20041211	13:03	12:57	13:40	?
20050325*2	16:41	16:37	17:16	?

20060413	11:41	11:12	12:04	?
20111112	05:10	05:18	06:00	?
20120102	00:44	00:59	01:52	?
20120503	00:59	01:16	02:19	?
20130602*2	01:57	02:10	02:26	?
20130903	17:02	16:46	17:45	?
20210424	22:16	22:22	23:05	?

*1: Identification of geomagnetic SC by both methods (=2), by only SYM-H (=1), and weak/unclear SC (=?)
*2: Reverse shock
*3: Density measurement is skeptical.

Table A4 Timing of IP detection and geomagnetic SC for SOHO-only 63 samples

Date	**SOHO**	**SYM-H**	**SC**[*1]
19960408	12:33	13:35	both
19970110	00:21	01:05	both
19970209	12:42	13:22	both
19970515[*3]	00:55	02:00	both
19970902	22:03	23:00	both
19971001	00:19	00:59	both
19971023	07:01	08:06	both
19971024	10:19	11:16	both
19971106	22:06	22:49	both
19971122	08:54	09:50	both
19971210	04:22	05:27	both
19971230	01:17	02:10	both
19980106	13:18	14:17	both
19980124	04:48	05:30	both
20000714	15:05	15:32	both
20000715	14:18	14:37	both
20001110	06:00	06:27	both
20010925[*3]	19:51	20:25	both
20011106[*3]	01:20	01:52	both
20011124	05:33	05:55	both
20040106	19:24	19:51	both
20050515	02:19	02:38	both
20050713	04:27	05:13	both
20050717[*3]	01:23	01:36	both
20050911	00:49	01:14	both
20110925	11:12	11:46	both
20120124[*2]	14:33	15:04	both
20120308[*3]	10:53	11:04	both
20130822	18:41	19:26	both
20141101	06:20	07:06	both
19960206	19:02	19:50	symH
19970111	04:27	05:16	symH
19970520	04:46	06:02	symH
19970903	08:11	08:56	symH
19971109	21:51	22:54	symH
19990628	02:28	02:59	symH
20000917	15:19	16:00	symH
20010118	09:18	10:12	symH
20030217	22:55	23:26	symH
20040122[*2]	08:45	09:22	symH
20040126	18:34	19:21	symH
20050429	15:31	16:06	symH
20050529	20:51	21:29	symH
20081028	19:44	20:10	symH
20160311	04:45	05:34	symH
20160725	01:15	02:12	symH
20220519	13:31	13:56	symH
19980131	15:56	16:44	weak
19980325	15:33	16:33	weak
19991204	00:47	01:31	weak
20000427	20:01	21:06	weak
20020326[*2]	10:13	10:50	weak
20030127	16:35	16:59	weak
20030311	15:46	17:16	weak
20030714	10:42	11:18	weak
20030726	12:36	13:06	weak
20031122	09:59	10:29	weak
20050508[*3]	09:07	09:34	weak
20061208	04:11	04:36	weak
20100908	01:07	02:18	weak
20150206	07:40	08:02	weak
20160311[*2]	19:18	19:47	weak
20201023	16:03	16:51	weak

*1: Identification of geomagnetic SC by both methods (=2), by only SYM-H (=1), and weak/unclear SC (=?)

*2: Reverse shock

*3: Density measurement is skeptical.